Published in final edited form as:

Nature. 2020 August ; 584(7822): 640–645. doi:10.1038/s41586-020-2447-x.

Cryo-EM of elongating ribosome with EF-Tu•GTP elucidates tRNA proofreading

Anna B. Loveland[1], **Gabriel Demo**[1,2], **Andrei A. Korostelev**[1,3,*]

[1]RNA Therapeutics Institute, Department of Biochemistry and Molecular Pharmacology, University of Massachusetts Medical School, 368 Plantation St., Worcester, MA 01605, USA.

[2]Present Address: Central European Institute of Technology, Masaryk University, Kamenice 5, Brno, 625 00, Czech Republic

[3]Lead contact

Summary

Ribosomes accurately decode mRNA by proofreading each aminoacyl-tRNA delivered by elongation factor EF-Tu[1]. Understanding the molecular mechanism of proofreading requires visualizing GTP-catalyzed elongation, which has remained a challenge[2–4]. Here, time-resolved cryo-EM revealed 33 states following aminoacyl-tRNA delivery by EF-Tu•GTP. Instead of locking cognate tRNA upon initial recognition, the ribosomal decoding center (DC) dynamically monitors codon-anticodon interactions before and after GTP hydrolysis. GTP hydrolysis allows EF-Tu's GTPase domain to extend away, releasing EF-Tu from tRNA. Then, the 30S subunit locks cognate tRNA in the DC, and rotates, enabling the tRNA to bypass 50S protrusions during accommodation into the peptidyl transferase center. By contrast, the DC fails to lock near-cognate tRNA, allowing dissociation of near-cognate tRNA during both initial selection (before GTP hydrolysis) and proofreading (after GTP hydrolysis). These findings reveal structural similarity between initial selection[5,6] and the previously unseen proofreading, which together govern efficient rejection of incorrect tRNA.

Keywords

translation elongation; decoding; proofreading; GTPase; time-resolved cryo-EM; elongation factor Tu

*Correspondence: andrei.korostelev@umassmed.edu.

Author contributions

Conceptualization: A.B.L, A.A.K. Methodology: A.B.L., G.D., A.A.K. Validation: A.B.L, A.A.K. Investigation: A.B.L., G.D. Resources: A.A.K. Writing- Original Draft: A.B.L, A.A.K. Writing- Review and Editing: A.B.L., G.D., A.A.K. Visualization: A.B.L. Supervision. A.A.K. Funding Acquisition: A.A.K.

Declaration of Interests

The authors declare no competing interests.

Introduction

A translating ribosome selects appropriate aminoacyl-tRNA and connects the incoming amino acid to the elongating peptide chain. Aminoacyl-tRNA (aa-tRNA) binds the ribosome as a ternary complex with elongation factor Tu (EF-Tu) and GTP (Fig. 1a; reviewed in refs[2–4]). tRNA selection involves two steps: initial selection and proofreading[1]. Initial selection discriminates against non-cognate tRNAs in the 30S A site before EF-Tu hydrolyzes GTP, allowing intact non-cognate aa-tRNA•EF-Tu•GTP ternary complex to dissociate from the ribosome[2–4]. GTP hydrolysis releases EF-Tu•GDP from the tRNA acceptor arm, which travels through the intersubunit space and inserts (accommodates) into the peptidyl transferase center (PTC) on the 50S subunit[7–9]. After GTP hydrolysis and before peptidyl transfer, the ribosome proofreads the aa-tRNA to reject incorrectly selected near-cognate aa-tRNA, preventing elongation with an incorrect amino acid [1,10,11].

Structural visualization of GTP-catalyzed decoding has remained a challenge, so high-resolution structures of decoding complexes have typically been captured by blocking GTP hydrolysis and elongation[5,6,12,13] (see Supplementary Discussion). Many structural steps remain to be captured to answer long-standing questions. First, it is unknown how the ribosome initially selects an incorrect near-cognate tRNA, but then rejects it by *proofreading* before forming a peptide bond. Next, it remains to be seen how GTP hydrolysis facilitates EF-Tu dissociation, and whether the dissociating EF-Tu could drive tRNA accommodation via a power-stroke-like mechanism[14]. Finally, it is unclear how tRNA bypasses structural obstacles[15] to allow its accommodation in the A site. To answer these questions, structural intermediates in the elongation pathway must be visualized using authentic substrates.

We used cryogenic electron microscopy (cryo-EM) to visualize an elongation event catalyzed by EF-Tu•GTP (Fig. 1a). Aminoacyl-tRNA was delivered as aa-tRNA•EF-Tu•GTP ternary complex to the 70S initiation ribosome programmed with a cognate or near-cognate mRNA codon in the A site. Cryo-EM data classification revealed numerous functional states (see Methods). We describe 17 structures of the ribosome with the cognate tRNA, at average resolutions from 3.0- to 4.0-Å (Fig. 1b and Extended Data Fig. 1), and 16 states of the near-cognate complex, at 3.3- to 4.3-Å average resolutions (Extended Data Fig. 2). The structural ensembles provide an unprecedented view of elongation (Video S1), including initial selection, GTP hydrolysis, conformational changes in EF-Tu, tRNA proofreading, tRNA accommodation, peptide bond formation, and pre-translocation. Comparison of cognate and near-cognate elongation uncovers the elusive mechanism of proofreading critical for translation fidelity.

Results and Discussion

Time-resolved cryo-EM reveals transient EF-Tu intermediates

To identify structural intermediates of elongation with *cognate Phe-tRNA*^{Phe}, we performed ensemble cryo-EM[16] of the EF-Tu•GTP-catalyzed reaction (Fig. 1a) at several time points, consistent with a biochemical time course for similar conditions [17] (Fig. 1c **and Methods**). Maximum-likelihood classification resolved distinct 70S functional states corresponding to substrates (i.e., vacant A site), EF-Tu-bound intermediates (i.e., A/T tRNA and EF-Tu), and

products of the decoding and elongation reactions (i.e., after EF-Tu release) (Fig. 1b–g and Extended Data Fig. 1). Over time, substrates decrease and products accumulate, whereas EF-Tu-bound states accumulate and then disappear, as expected for reaction intermediates (Fig. 1c). Our approach therefore captures long-pursued transient states of aminoacyl-tRNA delivery catalyzed by EF-Tu and GTP (Fig. 1d).

To visualize the structural intermediates of elongation, we focused on high-resolution maps from the 29-second time point (Extended Data Fig. 1, Table S1, Table S2 and **Methods**), when EF-Tu-bound particles reach a near-maximal level and peptidyl-transfer products begin to accumulate (Fig. 1c; see additional discussion in Methods). Most maps resolve near-atomic-resolution details (Fig. 1e–g) in the ribosome core, and lower-resolution features at the periphery, allowing interpretation of secondary-structure and/or domain rearrangements of EF-Tu (Extended Data Fig. 3, 4, 5, 8, 9). Six categories of structures describe distinct functional states (Fig. 1b): (I) substrates I-A and I-B, similar to A-site vacant 70S structures described before[18,19] (**Methods**), (II and III) EF-Tu-bound intermediates II-A to II-D and III-A to III-C (Fig. 2), (IV) tRNA accommodation-like states IV-A and IV-B (Fig. 3), (V) peptidyl-transfer classical states V-A and V-B (Fig. 3), and (VI) pre-translocation hybrid states VI-A and VI-B (Fig. 3). Collectively, the 17 structures suggest a pathway of cognate aminoacyl-tRNA from initial ribosome binding to accommodation to peptide-bond formation to pre-translocation (Fig. 1d and Video S1).

GTP hydrolysis gradually releases EF-Tu, while 30S adopts open and closed conformations

EF-Tu contributes to initial selection, proofreading [20] and tRNA accommodation [21], but the structural mechanisms of the latter two processes are unknown. Initial selection is achieved by separating the EF-Tu GTPase (domain 1) from the 50S sarcin-ricin loop (SRL) until the cognate tRNA is recognized in the 30S decoding center. Recognition of the tRNA anticodon causes a 30S-shoulder shift that docks EF-Tu at the SRL catalyzing GTP hydrolysis (see below and refs[5,6]). How EF-Tu rearranges and dissociates after GTP hydrolysis is less understood. Conflicting biochemical studies suggest that large-scale EF-Tu rearrangements occur on the ribosome [22] or after EF-Tu dissociation from the ribosome [23]. Further, it is not clear if EF-Tu dynamics facilitate spontaneous or power-stroke-driven accommodation of tRNA into the PTC [14] (Supplementary Information). Isolated EF-Tu adopts two globally different conformations: a compact GTP-bound and an extended GDP-bound form [24–26]. In the extended conformation, the GTPase domain is rotated by ~90°, concurrent with rearrangement of switch I and II regions (aa 38–64 and 83–97), which outline the GTP-binding pocket [24–26]. However, structures of ribosome-bound EF-Tu complexes have only described compact EF-Tu [5,6,12,13,27].

We find three categories of EF-Tu-bound states (9 maps), which suggest step-wise dissociation of EF-Tu from tRNA. (**1**) In five maps (II-A, II-B1, II-B2, III-A and III-B), EF-Tu adopts a compact conformation resembling the GTP-bound state, but featuring different conformations of switch regions indicating distinct states of the GTP-binding pocket (Fig. 2a–b and Extended Data Fig. 3a–f, m–n, p–q). Sub-classification reveals a subset of states, in which EF-Tu interacts with the N-terminal domain of L11 and with L7/L12 (Extended

Data Fig. 3s–v and Supplementary Information), consistent with stochastic binding of these 50S proteins [28]. (**2**) In three maps (II-C1, II-C2, III-C), EF-Tu adopts extended conformations resembling the GDP-bound state, with domain 1 (aa 1–200) released from domain 2 (aa 201–299) and rotated up to ~90° from its position in the compact conformation (Fig. 2c and Extended Data Fig. 3g–h, j–k, o, r). Despite dissociation of domain 1, the tRNA remains well-ordered because it is held in place by domain 2 (Extended Data Fig. 3w). (**3**) In one map (II-D), weak density for domain 3 (aa 300–392) continues to bridge the elbow of tRNA and the L11 stalk (Extended Data Fig. 3i,l), but domains 1 and 2 are not resolved. This map suggests that dynamic domain 1 and 2 have released from the tRNA's acceptor arm ((Extended Data Fig. 3x). II-D is therefore consistent with a late EF-Tu-dissociation and/or early tRNA-accommodation state.

Remarkably, ribosomes with compact and extended EF-Tu sample both open (II-A to II-D) and closed (III-A to III-C) 30S subunit conformations (Fig. 2d and Extended Data Fig. 4b–e). The tRNA adopts kinked A*/T (*A* site/*T*ernary on *open** 30S) and A/T (closed 30S) conformations, whose anticodon stem-loops are respectively loosely and stably bound in the 30S decoding center consistent with our previous work [5]. Rearrangement of the open to closed 30S states is coupled with movement of decoding-center nucleotide G530 toward A1492 and A1493 (Fig. 2d), as in Structures II (open) and III (closed) in previous work [5].

In all open 30S conformations with compact EF-Tu, the latter is separated from the SRL (II-A, II-B1 and II-B2). II-A has well-ordered switch I and II regions (Fig. 2e), and γ-phosphate is visible (Fig. 1e), consistent with functional states that precede GTP hydrolysis or phosphate release [24]. II-B1 and II-B2 have disordered switch I regions (Extended Data Fig. 3e–f), consistent with GDP bound to compact EF-Tu. II-C1 (Fig. 2c) and II-C2 have extended EF-Tu conformations (Extended Data Fig. 3g–h), which resemble isolated EF-Tu•GDP [25] on the path to EF-Tu dissociation.

In the closed 30S conformations, compact EF-Tu is closer to the SRL. In III-A, which appears to have intermediate domain closure, EF-Tu switch regions I and II are ordered, and EF-Tu tilts relative to the SRL (Extended Data Fig. 3m,p,y). The second, more-populated state III-B has a fully closed 30S and disordered switch I and II regions, representing a GDP-bound state after GTP hydrolysis (Fig. 2f and Extended Data Fig. 3n,q,y; [13,29,30]). Observation of compact EF-Tu in II-A and III-A is consistent with EF-Tu being separated from the SRL prior to GTP hydrolysis [5]. Structure III-B confirms that docking at the SRL, induced by the 30S closure, results in rapid GTP hydrolysis [27,31–35]. By contrast, III-C with the closed 30S contains extended EF-Tu (Extended Data Fig. 3o,r). Observation of extended EF-Tu in GDP states in both the open (II-C1 and II-C2) and closed (III-C) 30S conformations indicates continuous 30S sampling after GTP hydrolysis (Extended Data Fig. 3g, h, o).

Our data are consistent with the following model for EF-Tu rearrangements (Fig. 4a–e). Ternary complex initially binds the ribosome at the open-30S shoulder via EF-Tu, while tRNA samples the decoding center. Upon codon recognition, G530 (at the 30S shoulder), and A1492/A1493 (at the 30S body) rearrange, shifting the 30S shoulder and bringing EF-Tu closer to the SRL (Fig. 2b,d). In the closed 30S conformation, EF-Tu docks at the SRL

(Fig. 2f). The phosphate of A2662 of the SRL positions the conserved catalytic His84 of EF-Tu for GTP hydrolysis [5,27]. GTP hydrolysis and Pi release destabilize the switch regions of EF-Tu because they no longer interact with γ-phosphate[13,36]. When the switch regions refold, the β-hairpin conformation of switch I [25] (Fig. 2c and Extended Data Fig. 3j) becomes sterically incompatible with binding to tRNA, so GTPase domain 1 dissociates from aa-tRNA and the SRL. Domain 2 then dissociates from the CCA-end of aa-tRNA. Domain 3, which may be partially stabilized by the N-terminus of L11 and L7/L12 (Extended Data Fig. 3s–v and **Methods**), leaves last. The sequence of EF-Tu domain rearrangements is consistent with structural-dynamics simulations [21] and suggests that EF-Tu dissociation is unlikely to contribute to tRNA accommodation by a power-stroke-like mechanism[14].

As EF-Tu changes conformation, the 30S ribosomal subunit continues sampling the open conformation, wherein the decoding center loosens its “grip” on the codon-anticodon helix. The open 30S conformation is also observed in the absence of A-site tRNA, whereas the closed 30S conformation requires a bound anticodon stem-loop [37–39]. Thus, aa-tRNA•EF-Tu complex may dissociate from the ribosome with open 30S conformations, in either GTP- or GDP-bound states, consistent with biochemical studies proposing EF-Tu-dependent proofreading[20].

tRNA accommodation is coupled with 30S locking and rotation, and ASF movement

When EF-Tu dissociates, the aminoacyl-tRNA arm must traverse ~80 Å through the intersubunit space to accommodate into the PTC. Protrusions from the 50S subunit, however, form a narrow space for tRNA accommodation [40,41], and molecular-dynamics simulations showed that 23S rRNA helices, most notably H89 (residues 2454–2498) and the A loop (H92), occlude the tRNA path [15]. Our data reveal accommodation-like states (IV-A and IV-B) (Fig. 3, Extended Data Fig. 5c–f), which suggest that 30S rotation and A-site finger (ASF) movement allow the tRNA to bypass the occlusions. Importantly, the small subunit is closed in each accommodation state (Extended Data Fig. 4f). This indicates that EF-Tu dissociation substantially reduces the 30S opening dynamics with cognate tRNA, “locking” the tRNA into the decoding center.

Four representative structures differ in the positions of the tRNA relative to the A site (Fig. 3a–d and Extended Data Fig. 5a–h): (**1**) the A*/T tRNA upon EF-Tu release (II-D); (**2**) elbow-accommodated tRNA 1 (EA-1), close to A/T tRNA (IV-A); (**3**) elbow-accommodated tRNA 2 (EA-2), close to the accommodated A/A tRNA (IV-B); and (**4**) the CCA-accommodated A/A tRNA (V-A).

In II-D, the elbow of A*/T tRNA interacts with the L11 stalk, as described [5], and weak density for EF-Tu domain 3 concurs with EF-Tu dissociation prior to tRNA accommodation (Fig. 3a, Extended Data Fig. 3i,l). In the EA-1 pre-accommodation state (Fig. 3b), the elbow of tRNA (at C56 backbone) is shifted deeper into the ribosome—by ~40 Å—to interact with the long 50S hairpin loop called A-site finger (ASF; nucleotides 863–915 of helix 38, 23S rRNA; Fig. 3h). The acceptor arm of EA-1 (at A73 backbone) lies ~30 Å from the A*/T state and ~35 Å from the 50S A site. The 3′ terminal strand of EA-1 points at C2559 of H92, whereas the middle of the acceptor arm (at A64) is held in place by H89 via RNA

backbone-backbone packing (Fig. 3h and Extended Data Fig. 5c–d). EA-2 tRNA has bypassed H89, the CCA end is disordered, and the acceptor arm is ~7 Å from the position of A/A tRNA (measured at A73). Here, the acceptor arm is held in place near C2556 of H92 (Extended Data Fig. 5e–f). Both EA-1 and EA-2 are therefore transiently stabilized by interactions of the acceptor arm with different regions of H92.

In accommodation states IV-A and IV-B, the ribosome is rearranged relative to EF-Tu-bound states, allowing the tRNA to bypass the 23S rRNA obstacles and orient for CCA accommodation (Fig. 3b–c,h and Extended Data Fig. 5 compare a to c). First, the closed 30S subunit of pre-accommodation ribosomes is rotated by ~2.5°. This “partial accommodation rotation” (< 9° rotation observed in tRNA-mRNA translocation[2,42,43]) depresses the 30S A-site (at nt 35 of tRNA) by ~5 Å relative to H89, allowing the tRNA to pass under H89 (Fig. 3h). The abundance of partially-rotated ribosomes rises and decreases with time, indicating that partial rotation occurs at intermediate stages of the elongation event (Extended Data Fig. 6c). Second, the A-site finger moves by more than 10 Å to bind the tRNA elbow and stabilize the elbow-accommodated tRNAs (Extended Data Fig. 7i). This interaction confines the conformational dynamics of tRNA to allow the CCA insertion into the PTC.

Peptide bond formation and pre-translocation involve 30S subunit rotation

Four major states (V-A, V-B, VI-A, and VI-B) suggest the progress of the peptidyl transfer reaction, as discussed in Supplementary Information (Fig. 3d–g, Extended Data Fig. 6a–b, d–g). Briefly, V-A reveals a partial rotation of the 30S subunit (similar to that in accommodation IV-A and IV-B), which must be reversed for optimal alignment of aminoacyl-tRNAs in the PTC for peptidyl transfer to occur as in V-B (Extended Data Fig. 6a–b). Ensuing peptidyl transfer and E-tRNA release allow spontaneous 30S subunit rotation, resulting in formation of the canonical pre-translocation A/P and P/E tRNA hybrid states (VI-A) and elbow-shifted A/P* and P/E tRNAs (VI-B; Fig. 3f–g, Fig. 1g), consistent with many biochemical studies (reviewed in [2,43]). Partial non-cognate E-tRNA occupancy in the structures preceding VI-A and VI-B suggests no correlation between the occupancies of the E and A sites in the decoding, accommodation or peptidyl-transfer states (**Methods** and Extended Data Fig. 6j–m).

Near-cognate tRNA samples open 30S with and without EF-Tu

To understand the structural basis of tRNA selection, we repeated our cryo-EM analysis for a near-cognate complex formed with Phe-tRNA^{Phe} and an mRNA carrying a leucine codon (CUC) to create an A-C mismatch at the first codon position. Sixteen maps suggest an elongation trajectory that is overall similar to that of the cognate complex (Extended Data Fig. 2c, Supplementary Information). We focus on differences in particle distributions and structures that provide insights into the decoding mechanism. Although we used buffer conditions to maximize rare miscoding events (refs [20,44] and **Methods**), the distribution of particles in substrate, intermediate, and product states indicates that elongation remained less efficient than with the cognate tRNA. Near-cognate ribosomes with an empty A site (substrates) were 2-fold more abundant, whereas the A-tRNA-bound (product) ribosomes were 3-fold less abundant in comparison with the cognate complex (Extended Data Fig. 7a). Moreover, the near-cognate complex was depleted for GDP-bound EF-Tu (compact with

disordered switch I or extended conformations; Extended Data Fig. 7b) consistent with less efficient GTP hydrolysis [45,46]. Indeed, EF-Tu-bound states predominantly sample the open 30S subunit (Fig. 3l), similar to findings using GDPCP [5], indicating that anticodon stabilization, shoulder movement and EF-Tu docking at the SRL are less frequent than for the cognate ternary complex.

The most remarkable structural difference between near-cognate and cognate elongation complexes lies in the accommodation states. After EF-Tu dissociation, the accommodation EA intermediates with near-cognate tRNA continue to sample the open 30S conformation (IV-B1-nc) (Fig. 3i,l, Extended Data Fig. 5i–j), in contrast to cognate tRNA bound exclusively to the closed 30S subunit (Fig. 3l, Extended Data Fig. 4). Moreover, compared to the cognate EA tRNAs, the elbows of the near-cognate EA tRNAs contact the ASF deeper (Extended Data Fig. 7j), and density suggests a dynamic anticodon stem-loop in the 30S A site (Extended Data Fig. 5i–j). Upon CCA accommodation in the A site, a subset of near-cognate states also has an open 30S conformation (V-A1-nc (Fig. 3k, Extended Data Fig. 4j, Extended Data Fig. 7e and V-B1-nc (Extended Data Fig. 7g) and a disordered phenylalanine moiety, suggesting poor substrate positioning (Fig. 4k). Thus, a single mismatch perturbs the accommodation pathway of near-cognate tRNA. Sampling of the open 30S conformation is consistent with release of near-cognate tRNA during both initial selection (EF-Tu-bound) and accommodation, the latter step constituting EF-Tu-independent proofreading. Structural obstacles, including H89 and H92, likely facilitate tRNA dissociation during 30S rotational and opening dynamics.

The mechanism of proofreading

Our structural analyses reveal that initial selection and proofreading—long deemed biochemically separate events—are intertwined into a continuous process of mRNA decoding (Fig. 4). While GTP hydrolysis triggers EF-Tu release, our data are consistent with the idea that proofreading occurs both prior to and after EF-Tu dissociation, suggesting a revised mechanistic role for EF-Tu•GTP (Supplementary Information: Conformational proofreading). All three decoding steps—*initial selection* (pre-GTP hydrolysis; Fig. 4a–b), *EF-Tu-dependent proofreading* (post-GTP hydrolysis; Fig. 4c–e) and *EF-Tu-independent proofreading* (post-EF-Tu release; Fig. 4f–g) —rely on conceptually similar structural mechanisms. They involve the “locking/unlocking“ dynamics of the 30S decoding center, and steric hindrances induced by EF-Tu (during initial selection and EF-Tu-dependent proofreading) or by the protruding 50S rRNA (during accommodation). EF-Tu continuously destabilizes closure of the 30S subunit in both cognate and near-cognate complexes, before and after GTP hydrolysis. Destabilization of the closed 30S conformation likely arises from the strained conformation of the kinked A/T tRNA, whose anticodon stem-loop samples the decoding center while the CCA end remains pinned by EF-Tu at the 30S shoulder (Fig. 2a). Near-cognate tRNA is prone to dissociation from open 30S states during both initial selection (with EF-Tu•GTP) and proofreading (with EF-Tu•GDP) [20] because the mismatched mRNA-tRNA codon-anticodon helix is unstable in the decoding center. Cognate tRNA is retained by stabilizing interactions with decoding center nucleotides G530, A1492 and A1493 even in open 30S states (Fig. 2d and ref [5]).

After GTP hydrolysis and EF-Tu dissociation (Fig. 4a–e), the EF-Tu-independent stage of proofreading begins. Here, tRNA relaxes on its way toward the 50S A site (Fig. 4f). The ribosome—with 30S in a closed state—appears "committed" to accommodation of cognate tRNA, whose ASL is stably locked in the decoding center due to tRNA conformational relaxation, consistent with rapid accommodation and peptide-bond formation [31,47]. Partial rotation of the 30S subunit allows the tRNA to bypass rRNA protrusions and probably aids proofreading by delaying peptide bond formation until the 30S rotation is reversed (Fig. 4g–h). By contrast, ribosomes with an accommodating near-cognate tRNA continue to sample the 30S in open states (Fig. 4f–g, red arrows), which destabilize the near-cognate tRNA at two major points of contact: the decoding center and the ASF. Furthermore, 50S protrusions, including H89, likely destabilize the accommodating tRNA. Continuous sampling of open 30S restricts near-cognate tRNA entry into the PTC, consistent with tRNA rejection after EF-Tu release [11] and reduced rates for accommodation and peptide-bond formation [11,20]. Thus, minimization of miscoding events results from continuous verification of tRNA throughout the A*/T→EA→A/A trajectory. The universally-conserved decoding center and small-subunit dynamics therefore dictate high translation fidelity.

Cryogenic electron microscopy allowed us to resolve many transient intermediates in the course of a GTP-catalyzed reaction without the use of inhibitors. Recent advances in cryo-EM make it possible to rapidly apply samples to EM grids [48,49] and deconvolute heterogeneous ensembles of numerous structures at near-atomic resolution [16,50,51]. Together, these studies emphasize that high-resolution time-resolved cryo-EM could become the *bona fide* "structural biochemistry" method for visualizing complex biochemical pathways without inhibitors.

Methods

We performed ensemble cryo-EM [16] of EF-Tu•GTP-catalyzed delivery of *cognate aa-tRNA* at several time points. We incubated Phe-tRNA^{Phe}•EF-Tu•GTP ternary complex with *E. coli* 70S•fMet-tRNA^{fMet} programmed with mRNA carrying the initiation fMet (AUG) codon in the P site and Phe (UUC) codon in the A site (Fig. 1a). The reactions progressed on ice (to slow the reactions), were applied to cryo-EM grids, and were rapidly plunged into liquid ethane to stop their progress at different times (Fig. 1c and **Methods**). Datasets were collected for time points informed by a biochemical time course of the EF-Tu•GTP-catalyzed reaction under similar conditions [17].

Preparation and freezing of tRNA delivery complexes on cryo-EM grids

30S and 50S ribosomal subunits were prepared from MRE600 *E. coli* as described [52] and stored in Buffer A (20 mM Tris, pH 7, 10.5 mM $MgCl_2$, 100 mM NH_4Cl, 0.5 mM EDTA, 6 mM β-mercaptoethanol) at –80°C. mRNA containing the Shine-Dalgarno sequence and a linker to place the AUG codon in the P site and the Phe codon (cognate complex) or Leu codon (near-cognate complex) in the A site was synthesized by IDT DNA. Cognate complex mRNA was GGC AAG GAG GUA AAA AUG UUC AAA AAA, while near-cognate complex mRNA was GGC AAG GAG GUA AAA AUG CUC AAA AAA.

Components of ternary complex were prepared as follows. *E. coli* EF-Tu was prepared as previously described [5,53]. GTP was purchased from Roche. $tRNA^{Phe}$ and $tRNA^{fMet}$ were purchased from Chemblock. Cellular enzyme extract (S-100) was used for tRNA aminoacylation and was prepared from MRE600 *E. coli* as described[53]. Briefly, 2L of MRE600 *E. coli* culture in LB was harvested in log phase (OD 0.6) yielding approximately 5 g of cell pellet. The pellet was resuspended in 20 ml of S-100 Buffer (10 mM Tris, pH 7, 10 mM $MgCl_2$, 30 mM NH_4Cl, 6 mM β-mercaptoethanol) and the cells were lysed using a Microfluidics M-110P cell disruptor. The lysate was cleared by centrifugation at 15,000 rpm for 15 minutes at 4°C (JA-20 rotor, Beckman). Ribosomes from the cleared lysate were pelleted using ultracentrifugation in a Ti-70 rotor (Beckman) at 60,000 rpm, for 2 hours at 4°C. 2.5 g of DEAE cellulose (Sigma Aldrich) was equilibrated and washed three times with ice cold S-100 Buffer. Following the ultracentrifugation, the top 80% of the supernatant was transferred to the DEAE cellulose and allowed to mix for 30 minutes at 4°C. The DEAE cellulose was separated from solution by centrifugation in a table-top centrifuge at 5,000 rpm for 5 minutes at 4°C and the supernatant was removed. DEAE cellulose was washed with 40 ml of S-100 Buffer for 30 minutes at 4°C. The DEAE cellulose beads were isolated and mixed with 10 ml of S-100 Elution Buffer (10 mM Tris, pH 7, 10 mM $MgCl_2$, 250 mM NH_4Cl, 6 mM β-mercaptoethanol) for 30 minutes at 4°C. After centrifuging as before to separate the DEAE cellulose and supernatant, the supernatant was retained and used as the purified S-100 extract. $tRNA^{Phe}$ and $tRNA^{fMet}$ were charged using the S-100 extract supplemented with 0.1 mM Phenylalanine or Methionine, respectively, exactly as described in ref[53]. The methionine was formylated by including neutralized N10-formyl-tetrahydrofolate in the reaction[53]. Aminoacylation and formylation of tRNA were confirmed using acid gel electrophoresis[54], as shown in Extended Data Fig. 5q–r.

The 70S and ternary complexes were prepared as follows. Heat-activated (42°C, 5 minutes) 30S ribosomal subunits (3 μM) were mixed with 50S ribosomal subunits (3 μM) and with cognate or near-cognate complex mRNA (15 μM) (all final concentrations) in Reaction Buffer (20 mM HEPES•KOH, pH 7.5, 20 mM magnesium chloride, 150 mM ammonium chloride, 2 mM spermidine, 0.1 mM spermine) for 30 minutes at 37°C. A 2.25-fold molar excess of fMet-$tRNA^{fMet}$ was added to the ribosomal subunits and incubated for 5 minutes at 37°C. The 70S•mRNA•fMet-$tRNA^{fMet}$ complexes were diluted to 0.5 μM with Reaction Buffer and held on ice. Concurrently, the ternary complex of Phe-$tRNA^{Phe}$•EF-Tu•GTP was prepared as follows. 1.5 μM EF-Tu was pre-incubated with 1 mM GTP in Reaction Buffer for 5 minutes at 37°C and then was supplemented with 1.5 μM Phe-$tRNA^{Phe}$ (all final concentrations). After an additional minute at 37°C, the ternary complex was also kept on ice until plunging.

C-flat 1.2–1.3 (Protochips) holey-carbon grids coated with a thin layer of carbon (17 s, 29 s, 120 s cognate and 30 s near-cognate datasets) or Ultrathin Carbon Film on Lacey Carbon Support Film (Ted Pella) (0 s and 1800s cognate datasets) grids were glow discharged with 20 mA current with negative polarity for 45–60 s in a PELCO easiGlow glow discharge unit. A Vitrobot Mark IV was pre-equilibrated to ~4.5 degrees and 100% humidity for 1 hour prior to plunging. Pipettes, tips, tubes, and forceps were equilibrated on ice for 30 minutes prior to the beginning of the plunging procedure and kept on ice when not in use during the procedure. For each grid, 1.5 μL of 70S•mRNA•fMet-$tRNA^{fMet}$ was mixed with 1.5 μL of

ternary complex with ice-chilled tips and in an ice-chilled tube. ~10 seconds prior to the desired time point, the reaction was transferred from the tube in an ice-chilled tip into the Vitrobot chamber, quickly applied to a chilled Holey-carbon grid, and then blotted for 4 s prior to plunging into liquid-nitrogen-cooled liquid ethane. The time point when the grid hit the ethane was noted as the reaction duration. The cognate data presented are from grids prepared from the same half reactions and plunged at 17 s, 29 s, and 120 s within 30 minutes of each other. The near-cognate data is from a grid prepared at the same plunging session, using the same ternary complex preparation with ribosomes programmed with the Leu-encoding mRNA. The 0 s and 1800 s data were prepared using the same procedure, with buffer used instead of ternary complex for the 0 s timepoint. The final reactions on the grids had the following concentrations: 250 nM 50S; 250 nM 30S; 1.25 μM mRNA; 560 nM fMet-tRNA^{fMet}; 0.75 μM EF-Tu; 500 μM GTP, and 0.75 μM Phe-tRNA^{Phe}.

Electron Microscopy

Data for the cognate tRNA delivery complexes at 0, 17, 29, 120 and 1800 s and near-cognate complex at 30 s were collected on a Titan Krios electron microscope (FEI) operating at 300 kV and equipped with a Gatan Image Filter (GIF) and a K2 Summit direct electron detector (Gatan Inc.) targeting 0.3 to 2.0-μm underfocus. For the cognate, 29-s time point, a dataset of 678,268 particles from 3218 movies was collected automatically using SerialEM [55]. Similarly, for the cognate complex data were collected as follows: 0-s, 7,428 particles from 67 movies; 17-s, 375,869 particles from 1640 movies; 120-s, 127,089 particles from 666 movies; and 1800-s, 13,126 particles from 167 movies. For the near-cognate complex, one 30-s time point was similarly collected and included 565,412 particles from 2508 movies. For each data collection, 35–36 frames per movie were collected at 1 $e^{-}/Å^2$ per frame for a total dose of 35–36 $e^{-}/Å^2$ on the sample. The super-resolution pixel size was 0.667 Å on the sample as calibrated from cross-correlation of the atomic model of PDB: 5UYL or 5UYM [5] to the maps for Structures II-A and III-B, respectively, using Chimera.

Image processing

Particles were extracted from aligned movie sums as follows. Movies were processed using IMOD [56] to decompress frames, apply the gain reference, and to correct for image drift yielding image sums with pixel size of 1.333 Å. CTFFIND4 [57] was used to determine defocus values. Particles were automatically picked from 5×-binned images using Signature [58] with a ribosome reference (18 representative reprojections of the EM databank map 1003 [59]). 288 × 288-pixel boxes with particles were extracted from motion-corrected images, and assembled into stacks in EMAN2 [60]. To speed up processing, 2×- and 4×-binned image stacks were prepared using resample.exe, which is part of the Frealign distribution [61].

Optimization of grid preparation for time-resolved cryo-EM

The conditions for complex preparation, grid freezing, and data collection were optimized to yield the conditions described in the above sections. Using small datasets (10,000–50,000 particles), we tested different plunging approaches, including a manual plunger and CP3 (Gatan Inc.) operating in a cold room (Brandeis University Cryo-EM facility); Vitrobot Mark IV (UMass Medical School Cryo-EM core facility), different grid types (holey carbon grids or carbon-coated holey carbon grids), reaction duration (4 s to 60 s), temperature (up to

10 degrees Celsius), reaction conditions (varying ternary complex to ribosome ratio and buffer composition) and dataset size. Datasets were collected on F20 or F30 electron microscopes at Brandeis University. The datasets were processed using procedures described above and classified as described below but were modified to allow for the different microscopes and detectors used. We observed the following trends. The CP3 plunger allowed us to achieve fastest reaction times from mixing to plunging within 4 seconds, but suffered from poor temperature control and inconsistent grid quality due to fast handling. We observed ~5% occupancy of EF-Tu and ~10% accommodated A-tRNA in these early experiments and were gratified to learn that 15–30 s time points led to increased populations of intermediates. Use of holey carbon or carbon-coated holey carbon grids yielded approximately equivalent EF-Tu loading onto ribosomes after correcting for ribosome density (typically, 7-times higher concentrations of the 70S complexes were used for holey carbon grids). Use of carbon-coated grids, however, yielded more consistent ice thickness and higher-resolution reconstructions.

To test whether EF-Tu occupancy estimation at different time points could be biased due to the variation in dataset sizes, we analyzed 10 smaller datasets (~20,000 to ~50,000 particles) from reactions quenched at 20 to 30 seconds. Data classification consistently revealed EF-Tu at 10–20% occupancy, ruling out the bias.

Classifications

In parallel with the classification approach shown in Extended Data Fig. 1 and 2 and described in detail below, we performed over 100 classifications that differed by the number of classes (from 2 to 48), number of classification steps, masking approaches (3D mask and spherical focus mask in Frealign), mask positions and sizes (30S, A-site, A- and P-sites, PTC, L11 stalk etc.) and resolution cutoffs (ranging from 12 Å to 4 Å). These classifications resulted in more than 1,000 maps, which generally reproduced the classes discussed in the main text. The classifications revealed different positions of the mobile parts of the ribosome, including the L1 and L11 stalks. We discovered additional features, which are consistent with elusive interactions between EF-Tu and a highly dynamic L7/L12 stalk, implicated in recruiting the ternary complex to the ribosome [28,62], as described in Supplementary Information and Extended Data Fig. 3s–v.

Distribution of states

Extensive maximum-likelihood classification of datasets at different time points was performed to identify the intermediates that might characterize substrate-like, EF-Tu-bound, accommodation, peptidyl transfer and pre-translocation sub-states (Fig. 1b). EF-Tu-bound particles were found at similar abundance at the early time points (up to 30 sec) in smaller and large datasets, ruling out a bias in the classification and abundance estimation due to dataset size and clearly fell in the 120s time point (see above). We observed no A/A, EA or A/P tRNA (product) states at the 0-second time point. The presence of these states upon addition of the ternary complex (at 17 s, 30 s and 120 s), in which EF-Tu was present in excess over aa-tRNA, demonstrates that the decoding, accommodation, peptidyl-transfer and pre-translocation states result from interaction with the ternary complex and are not due to pre-bound or spontaneously re-binding tRNA in the initial 70S ribosome sample.

The extent of partial 30S subunit rotation, which is associated with tRNA accommodation upon EF-Tu release (Fig. 3h), reduces with time (Extended Data Fig. 6c), consistent with accommodation being a slow and potentially rate-limiting step [31]. By contrast, ribosome populations within EF-Tu-bound states (Structures II-A to II-C2 and III-A to III-C) at 17 and 120 seconds are similar to those at 29 seconds. This suggests that interconversions among EF-Tu-bound states occur with fast rates, and involve ribosomes that bind the ternary complex at earlier and later time points. At the later time points, EF-Tu-bound intermediates likely report on ribosomes that proceeded through multiple cycles of binding and dissociation of EF-Tu ternary complex, and/or dissociation of the accommodating tRNA. Similarly, the distribution of product states in non-rotated and rotated 70S conformations (Structures V and VI) remain similar with respect to each other, consistent with fast interconversions observed by FRET studies [63].

High-resolution classifications, map refinement and reconstruction

FREALIGN v9.11 was used for most steps of refinement and reconstruction [61] (Extended Data Fig. 1 and 2). 4×-binned image stacks were initially aligned to a ribosome reference [59] (EM databank map 1003) using three rounds of mode 3 (global search) alignment, including data in the resolution range from 300 Å to 20 Å. Next, the 2× and later unbinned image stacks were successively aligned against the common reference using mode 1 (local refinement), including data up to a high-resolution limit of 6 Å (Cognate 17 s, 29 s, 120 s, Near-cognate 30 s) or 8 Å (Cognate 0 s, 1800 s). Subsequently, the refined parameters were used for classification of 4×-binned stacks into 8 classes (Cognate 0 s, 17 s, 29 s, 1800s) or 20 classes (Cognate 120 s or Near-cognate 30 s) in 50 rounds using a spherical (50-Å radius) focus mask around EF-Tu and A/T tRNA, including resolutions from 300 to 12 Å during classification. This classification (*Classification 1*) separated ribosomes in the classical and hybrid state from 50S subunits, and in each case included one class with density for EF-Tu.

Classification of cognate EF-Tu states—To find an optimal strategy to resolve distinct states of EF-Tu-containing particles, we compared individual classifications of the 17-, 29-, and 120s datasets against that of a combined stack of EF-Tu-containing particles (as described in the next paragraph). We independently classified EF-Tu-containing classes of the 17-, 29-, and 120-second datasets, using a 3D mask around the 30S shoulder domain and then a 30-Å focus mask centered around EF-Tu, as described below. We have also tested classifications with other masks encircling EF-Tu. These approaches and analyses of dozens of maps revealed that individual EF-Tu-containing states are structurally similar between these three datasets, revealing independently: the 30S domain closure, EF-Tu movements and domain rearrangements. This result suggested that similar structural states are sampled in the course of reaction, and that we might be able to improve the resolution of the final maps by combining these data. Indeed, classifications of the combined datasets have reproducibly improved the density for EF-Tu, and the average resolutions for EF-Tu-containing classes have improved by 0.1–0.3 Å. Map improvements were confirmed by visual inspections of the densities originating from the 17s, 29 s and the combined datasets.

The particles bound with EF-Tu in Classification 1 of the cognate datasets were extracted using merge_classes.exe including particles with >50% occupancy and scores >0 (29,453

particles at 17 s, 47,421 particles at 29 s, and 2,964 particles at 120 s). These stacks were appended and all 79,838 particles were processed together to increase resolution of the final classes as described above. The joint stack was first aligned by running 3 rounds of mode 1 refinement including resolution from 300 to 8 Å during refinement. Next, the particles were separated into two classes using a 3D mask that included the shoulder domain of the 30S subunit to separate particles with an open 30S from those with the closed 30S conformation. Two new stacks were prepared and further subclassified into 4 (closed 30S) or 6 classes (open 30S) using a small focus mask (30 Å) centered around EF-Tu using data up to 12 Å resolution for classification only (Extended Data Fig. 1b). After 50 rounds of classification, maps were prepared from the unbinned stack and used without further orientation refinement. Eight of these 10 classes were modeled and refined and are described in the text as structures II-A, II-B1, II-B2, II-C1, II-C2, III-A, III-B, and III-C. To obtain the best possible map of the EF-Tu release state (II-D), the open 30S particle stack was separated into 10 classes using a larger focus mask (60 Å) centered at EF-Tu. This classification separated out particles that were interacting with L11 and L7/L12 in different ways (Extended Data Fig. 3s–v), particles in which EF-Tu was close to other ribosomes (not shown), and a cleaner release intermediate state which was fit as state II-D.

Classification of accommodation and peptidyl transfer intermediates— Classical-state 70S classes (with non-rotated or partially-rotated 30S) with either 2 tRNAs and a weak ASL in the A site or 3 well-ordered tRNAs from Classification 1 were merged using merge_classes.exe including particles with >50% occupancy and scores >0 (201,764 particles) and were further subclassified into 24 classes using a 46-Å focus mask around the A and P sites of the 30S and 50S ribosomal subunits using data up to 12 Å resolution (Extended Data Fig. 1a). After 250 rounds of classification, 13 classes contained three tRNA, 3 classes were accommodation or intermediates, 5 classes had empty A sites in the classical (4) or hybrid (1) conformation, and 3 classes were low resolution. The particles from the 13 classes with three tRNA were extracted using merge_classes.exe including particles with >50% occupancy and scores >20 (83,981 particles) and separated into two classes using the same 46-Å focus mask, 50 rounds, and data to 12 Å. This classification yielded maps corresponding to models V-A and V-B. These classes were extracted for further exploratory subclassifications (see Supplementary Information) and were independently refined to improve map resolution. Particles belonging to the accommodation intermediate with the elbow at the A-site finger and a disordered acceptor arm were extracted using merge_classes.exe including particles with >50% occupancy and scores >0 (8,072 particles) and were separated into five classes using a 30-Å focus mask centered around the disordered acceptor arm using 50 rounds and data to 12 Å resolution. Two of these maps with the best features are modeled as states IV-A and IV-B.

Classification of hybrid states—The hybrid-state particles (with fully rotated 30S) from Classification 1 were also extracted using merge_classes.exe including particles with >25% occupancy and scores >0 (141,604 particles) and were further subclassified into 8 classes using the same 50-Å focus mask as Classification 1 (Extended Data Fig. 1a). After 50 rounds of classification, 2 classes contained two tRNAs (one dipeptidyl-tRNA in A/P site and one deacylated tRNA in the P/E sites differing the position of A/P tRNA elbow) similar

to states VI-A and VI-B. The 6 remaining classes contained one tRNA in the P/E conformation, and the class with the best resolved features was modeled as class I-B. Limiting the hybrid-state particle stack to those particles with >50% occupancy and scores >20 from Classification 1 and repeating the classification, yielded the product ribosome states exhibiting higher resolution features in the PTC, and ultimately these were modeled as states VI-A and VI-B.

Classification of the partially occupied E site—To investigate the occupancy of the E site, we used maximum likelihood classification of the 29-s particle substack within a 30-Å focus mask centered on the E-site. To this end, the substrate-like particles (non-rotated 70S with empty A site, 104,795 particles), EF-Tu-containing particles with the domain-open 30S (24,120 particles), EF-Tu-containing particles with the domain-closed 30S (15,216 particles), elbow-accommodation particles (8,072 particles), and peptidyl-transfer-like particles (83,981 particles) (see Extended Data Fig. 1a) were separately classified into 8 classes for 50 rounds, using data up to 12-Å resolution. In each case, 1–2 classes contained no E-tRNA and 0–1 classes contained weak tRNA-elbow-like density at the L1 stalk with no density for the acceptor arm and ASL. The population of the weak/vacant E-site is constant (~20–25%) among the substrate-like, EF-Tu-bound, accommodation and peptidyl-transfer states. The maps with the vacant and tRNA-bound E site were similarly resolved. In the E-tRNA bound states, non-cognate tRNA does not base-pair with the E-site codon (AAA), similarly to that in previous structures[64]. Unlike the well-resolved P-site and A-site tRNAs, the identities of the E-tRNA nucleotides could not be unambiguously ascribed to $tRNA^{fMet}$ or $tRNA^{Phe}$ due to lower resolution, consistent with conformational and compositional heterogeneity. Both particle populations and visual inspection of the maps with the vacant E and tRNA-bound E site do not reveal obvious correlations with the occupancy or with structural features of the 30S A site or EF-Tu, suggested by the allosteric three-site model [65,66]. Although our observations are consistent with biochemical [67,68] and biophysical[69] findings of the absence of the allosteric interaction between the E and A sites, non-cognate E-tRNA in our study prevents direct addressing of the allostery hypothesis.

Classification of the near-cognate dataset—The near-cognate dataset was processed in a similar fashion (Extended Data Fig. 2a) except that the EF-Tu-bound particles were processed independently and 3D masking of the shoulder separated states nc-IV and nc-V. First, EF-Tu-bound particles from Classification 1 were extracted using merge_classes.exe including particles with > 50% occupancy and scores > 0 (11,091 particles). Multiple strategies were tried to find particles with a closed 30S domain. First, the particles were separated into two or four classes using a 3D mask that included the shoulder domain of the 30S subunit. While classes with an intermediate domain closure were apparent, no class with a fully closed 30S domain with residues 1492 and 1493 in the ON conformation emerged. Alternatively, a small focus mask (30 Å radius) around EF-Tu was used to separate particles into 4–8 classes based on EF-Tu features. Classification was limited to 12 Å resolution and 50–100 rounds. Classification into 6 models yielded the most interpretable classes. These classes revealed EF-Tu conformations such as GTP-like conformation with an ordered or disordered switch I region, the extended post-hydrolysis conformation, and a pre-release conformation including a weak domain 2 matching those previously observed in the cognate

data. In this classification too, none of the near-cognate EF-Tu maps had a closed 30S conformation. To quantify differences between EF-Tu states in the near-cognate and cognate datasets, the cognate 29 s data was processed identically to near-cognate 30 s dataset using 6 models and the 30-Å focus mask. In addition to the classes described above for the near-cognate, a class with EF-Tu at the SRL and the 30S in the closed conformation was readily apparent in the cognate dataset. The percentage of 70S particles assigned to these classes is quantified in Fig. 3l and Extended Data Fig. 7b. Separation of near-cognate accommodation and peptidyl transfer states benefitted from a 3D mask around the shoulder domain of the 30S rather than focus masks as used in the cognate dataset. This type of classification revealed differences in the rotation of the 30S and 30S domain opening. To answer if domain opening occurs during accommodation with cognate tRNA (Fig. 3l), particles belonging to the cognate 29 s elbow accommodation states were also separated with the 3D mask around the shoulder into either 2 or 6 classes, but an open 30S was not observed.

Assessing optimal reconstruction parameters for low-population classes (< 10,000 particles) using: (a) a test with simulated stacks; and (b) classes II-A and IV-A

(a) Test with simulated stacks: Because our classifications yielded several classes comprising less than 10,000 particles (see below), we tested which approach to particle parameter (orientation and shift) refinements yields most resolved maps. Specifically, we asked how the maps with original particle orientation parameters (i.e. *entire stack aligned together then no orientation refinement after classification*) compare with those, in which particle orientation parameters are *refined after classification*. Here, we describe a simulation, in which we also asked whether and how the number of particles affects the resolution of the maps. To this end, we tested three approaches, employing Frealign v9.11, cisTEM −1.0.0-beta [70] and Relion-3-beta [71] to process particle stacks with different numbers of particles. To ensure that the different particle stacks contain particles with similar structural features (i.e. the same Structure class) to allow map comparisons, they were generated from a single large high-resolution stack of 31232 particles (class V-A; 3.2 Å average resolution) in triplicates, yielding stacks of approximately 500, 1000, 2000, 4000, 8000, and 16000 particles (18 stacks in total). To this end, the occupancy column of the Frealign parameter file was replaced with random numbers from 0–100, and the stacks and parameter files of appropriate sizes were extracted by varying the occupancy threshold using merge_classes.exe.

For each substack, we next obtained reconstructions using: 1) FrealignX_calc_reconstruction (using the original particle orientation parameters determined before classification), 2) cisTEM's autorefine procedure with "Initial Res. Limit" set either to (a) 60 Å to match initial resolution in the Relion procedure or to (b) 50 Å, which resulted in improved maps for small stacks; or 3) Relion 3D autorefine procedure with default parameters. Procedure 1 is identical to our typical map calculations, described above, in that the original refinement (orientation and shift) parameters were used to create 1x binned reconstructions. Procedures 2a and 2b in cisTEM were used to determine and refine the orientation and shift parameters independently for each substack, using default cisTEM settings. The reference for particle alignment was EMD-1003 prepared in EMAN2 by

changing pixel size. Procedure 3 in Relion was performed with default settings to determine the orientation and shift parameters and limit data resolution according to “gold-standard” settings. The reference for particle alignment was filtered to 60 Å as per default settings in Relion. For all procedures, the final resolution was obtained from the masked reconstruction (FSC_part in Frealign/cisTEM or Post-Process step in Relion), without additional beam-tilt or other corrections.

This test revealed that the average map resolutions decrease with the decreasing number of particles, consistent with published results[72]. Importantly, post-classification particle parameter refinement (procedures 2 and 3) is detrimental for smaller stacks, resulting in poorly resolved maps, as described in the next paragraph. Furthermore, the resolutions estimated from triplicate stacks are highly variable for small stacks (ranging from 6 to 21 Å for 1000 and 500 particles), further emphasizing suboptimal particle parameter refinement when the particle numbers are low. Instead, original orientation parameters (procedure 1) result in interpretable maps with well-resolved features even for 500 particles (~4.84±0.09 Å resolution).

By contrast, for the reconstructions calculated for the full large stack of 31,232 particles with the original and refined particle parameters, the map quality and resolutions were similar: 3.40 Å (procedure 1), 3.37 Å (procedure 2) and 3.76 Å (procedure 3). Relion’s performance may be suboptimal in our tests because we have not used the complete particle-picking and data processing pipeline in Relion, to ensure that the same particles are used here in all three procedures. Nevertheless, the trends observed for Relion-processed data were similar to those for Frealign and CisTEM. In general, our classification attempts in GPU-accelerated Relion with default parameters have yielded high-quality initial reconstructions, similar to those in Frealign and cisTEM, but have not separated the classes as efficiently as Frealign. Frealign was more time-efficient than cisTEM or Relion, allowing us to test and compare numerous classification approaches, and thus representing an optimal classification strategy.

Maps with the original and refined particle parameters differed most for the stacks with less than 4,000 particles. At 4,000 particles, the resulting maps show similar resolutions for procedures 1 and 2a and 2b (3.87±0.02 Å (1), 3.97±0.05 Å (2a) and 4.06±0.05 Å (2b), respectively) and a lower resolution for procedure 3 (5.01±0.03 Å). Maps obtained for 2000 particles had substantially more diverging resolution estimates from the triplicates in each approach, and particle-parameter refinement yielded less resolved maps (4.14±0.05 Å (1), 4.53±0.11 Å (2a), 4.37±0.06 (2b) and 6.7±0.07 Å (3)). At 1000 and 500 particles, the differences in resolution and map quality were even more pronounced (1000 particles: 4.46±0.06 Å (1), 14.12±7.5 Å (2a), 5.21±0.2 (2b) and 9.22±0.2 Å (3); 500 particles: 4.84±0.09 Å (1), 20.5±1.3 Å (2a), 8.0±4.1 (2b) and 12.3±2.6 Å (3)). Visual inspection of the small-stack maps confirmed that the procedure employing original refinement parameters (1) resulted in superior maps, which retained some higher-resolution features such as RNA nucleotide separation, unlike the procedures with orientation parameters refined for individual substacks (2a, 2b and 3).

(b) Refinement of particle parameters for II-A and IV-A: In parallel with the simulation test, we tested the three reconstruction and refinement procedures described

above on the classification-derived states with different numbers of particles: II-A (7,320 particles) and IV-A (1,471 particles). Similarly to the simulation results for the least-populated stacks, reconstructions for the sparse class IV-A are most well resolved with the default original particle parameters, whereas post-classification particle parameter refinement is detrimental to map quality. Specifically, our default reconstruction with subsequent beam-tilt corrections yielded a 4.0 Å (average resolution) reconstruction (map 1). Visual inspection confirmed that local features correspond to this average resolution, with some regions containing higher-resolution features, such as separated stacked nucleotides. Being part of the larger stack, the particles in this class have partial occupancies (calculated by frealign_run_refine in the original refinement procedure), and frealign_calc_stats reports they correspond to 1471 particles. To test particle parameter refinement in cisTEM (procedure 2) and Relion (procedure 3), we extracted particles belonging to state IV-A using merge_classes.exe including particles with >50% occupancy and scores >0, yielding a 1790 particle stack with occupancies reset to 100%. This stack was imported with CTF parameters into cisTEM and refined against EMD-1003 using default autorefine parameters, followed by beam-tilt correction, yielding a map at 4.63 Å resolution (map 2). Similarly we exported the stack and par file to Relion and performed 3D-autorefine against EMD-1003 as a reference using default parameters, followed by beam-tilt refinement, 3D-autorefine and post-processing (all steps in Relion), yielding a 6.61 Å reconstruction (map 3). Both cisTEM and Relion maps contained similar lower-resolution features, including EA-1 tRNA, but lacked high-resolution detail, indicating suboptimal particle parameter refinement, likely due to the small particle number. Indeed, for the modestly populated class II-A of more than 7,000 particles, the map resolutions and structural details were improved to: 3.6 Å (procedure 1), 3.8 Å (procedure 2) and 4.9 Å (procedure 3). Nevertheless, visual inspection confirmed that both the highly resolved regions (e.g. peptidyl transferase center) and less resolved features (e.g. secondary structure of peripheral proteins) were superior in map 1 obtained with the original particle parameters.

Finalizing maps—After the final classifications were completed, we were able to improve each map by 0.1–0.4 Å by applying a beam tilt correction using cisTEM [70]. The beam tilt parameters were calculated once for each dataset using all particles and then were applied to the classified maps. In the case of EF-Tu, where 3 datasets were joined, the beam tilt parameters were calculated using the 79,838 EF-Tu bound particle stack then applied to each of the 10 classes described in the text.

FSC curves were calculated by FREALIGN (FSC_part) for even and odd particle half-sets (Extended Data Fig. 1c–f, 2b). The maps used for structure docking and refinement were softened or sharpened by using bfactor.exe, part of the FREALIGN v9.11 distribution.

To assess the local resolution of the cryo-EM maps and filter them for structure refinements, we used blocres and blocfilt from the Bsoft package[73], after testing several local-resolution filtering approaches. Briefly, a mask was created for each map by low-pass filtering the map to 30 Å in Bsoft, then binarizing, expanding by 3 pixels and applying a 3-pixel Gaussian edge in EMAN2. Blocres was run with a box size of 26 pixels for maps with average resolutions near 4 Å, or a box size of 20 pixels for maps I-A, V-A, V-B, VI-A, and VI-B with resolutions closer to 3 Å. In each case, the resolution criterion was FSC with cutoff of

0.143. The output of Blocres was used to filter maps according to local resolution using blocfilt. Visual inspections and structure refinements against (1) original Frealign maps, (2) blocfilt maps and (3) blocfilt maps followed by filtering with different B-factors at different resolutions revealed that optimal balance between high-resolution and lower-resolution regions is achieved for blocfilt maps filtered with a constant B-factor of −50 $Å^2$ to the average resolution as determined by FSC_part. These maps were used for final structure refinements (Tables S1, S2, S3). Local regions described in the manuscript were nevertheless inspected using a series of maps (for each class) obtained with different filtering approaches to minimize bias in interpretation.

Model building and refinement

The 3.2-Å cryo-EM structure of 70S•tRNA•EF-Tu•GDPCP (PDB: 5UYM, [5]) was used as a starting model for structure refinements. A*/T for Structures II-A to II-D was adopted from PDB: 5UYL [5]). The starting model for domain 1 of EF-Tu bound with GDP was taken from PDB: 1DG1 [74]. The starting models for the EA, A/A, and A/P $tRNA^{Phe}$ were adapted from PDB: 1VY5 [75]. fMet and Phe and fMet-Phe dipeptide were adapted from PDB: 1VY4 and PDB: 1VY5 [75]. E-site tRNA was modeled as $tRNA^{fMet}$ [5]. E/P $tRNA^{fMet}$ was modeled using PDB: 4V80 [76] while H69 of 23S rRNA in the hybrid states was modeled using PDB: 4V9D [18]. All Structures were domain-fitted using Chimera [77] and refined using real-space simulated-annealing refinement using RSRef [78,79] against corresponding maps. Local structural elements that differed between structures, such as the decoding center or mRNA codon, were manually fitted and modeled into cryo-EM maps in PyMol [80] and Coot [81]. Refinement parameters, such as the relative weighting of stereochemical restraints and experimental energy term, were optimized to produce the optimal structure stereochemistry, real-space correlation coefficient and R-factor, which report on the fit of the model to the map [82]. Lower-resolution (~4 Å) structures were refined conservatively and visual inspection confirmed good fits. Secondary-structure restraints, comprising hydrogen-bonding restraints for ribosomal proteins and base-pairing restraints for RNA molecules were employed as described [83] and allowed for a conservative and stereochemically-restrained refinement into lower-resolution maps. The structures were next refined using phenix.real_space_refine [84] followed by a round of refinement in RSRef applying harmonic restraints to preserve protein backbone geometry [78,79]. Phenix was used to refine B-factors of the models against their respective maps [84]. The resulting structural models have good stereochemical parameters, characterized by low deviation from ideal bond lengths and angles and agree closely with the corresponding maps as indicated by high correlation coefficients and low real-space R factors (Tables S1, S2 and S3). Visual inspection of key functional regions was performed for each structure to ensure reasonable fits.

Structure superpositions and distance calculations were performed in PyMol. To calculate an angle of the 30S subunit rotation for accommodation and peptidyl-transfer states with respect to Structure III-B, 23S rRNAs were aligned with 23S rRNA from Structure III-B using Pymol, and the angle between 16S body regions (residues 2–920 and 1398–1540) was measured in Chimera. Figures were prepared in PyMol and Chimera.

Data Availability

The models generated and analyzed during the current study will be available from the RCSB Protein Data Bank: 6WD0 (Structure I-A), 6WD1 (Structure I-B), 6WD2 (Structure II-A), 6WD3 (Structure II-B1), 6WD4 (Structure II-B2), 6WD5 (Structure II-C1), 6WD6 (Structure II-C2), 6WD7 (Structure II-D), 6WD8 (Structure III-A), 6WD9 (Structure III-B), 6WDA (Structure III-C), 6WDB (Structure IV-A), 6WDC (Structure IV-B), 6WDD (Structure V-A), 6WDE (Structure V-B), 6WDF (Structure VI-A), 6WDG (Structure VI-B), 6WDH (Structure IV-B1-nc), 6WDI (Structure IV-B2-nc), 6WDJ (Structure V-A1-nc), 6WDK (Structure V-A2-nc), 6WDL (Structure V-B1-nc), and 6WDM (Structure V-B2-nc). The cryo-EM maps used to generate models will be available from the Electron Microscopy Database: EMD-21619 (Structure I-A), EMD-21620 (Structure I-B), EMD-21621 (Structure II-A), EMD-21622 (Structure II-B1), EMD-21623 (Structure II-B2), EMD-21624 (Structure II-C1), EMD-21625 (Structure II-C2), EMD-21626 (Structure II-D), EMD-21627 (Structure III-A), EMD-21628 (Structure III-B), EMD-21629 (Structure III-C), EMD-21630 (Structure IV-A), EMD-21631 (Structure IV-B), EMD-21632 (Structure V-A), EMD-21633 (Structure V-B), EMD-21634 (Structure VI-A), EMD-21635 (Structure VI-B), EMD-21636 (Structure IV-B1-nc), EMD-21637 (Structure IV-B2-nc), EMD-21638 (Structure V-A1-nc), EMD-21639 (Structure V-A2-nc), EMD-21640 (Structure V-B1-nc), and EMD-21641 (Structure V-B2-nc).

Extended Data

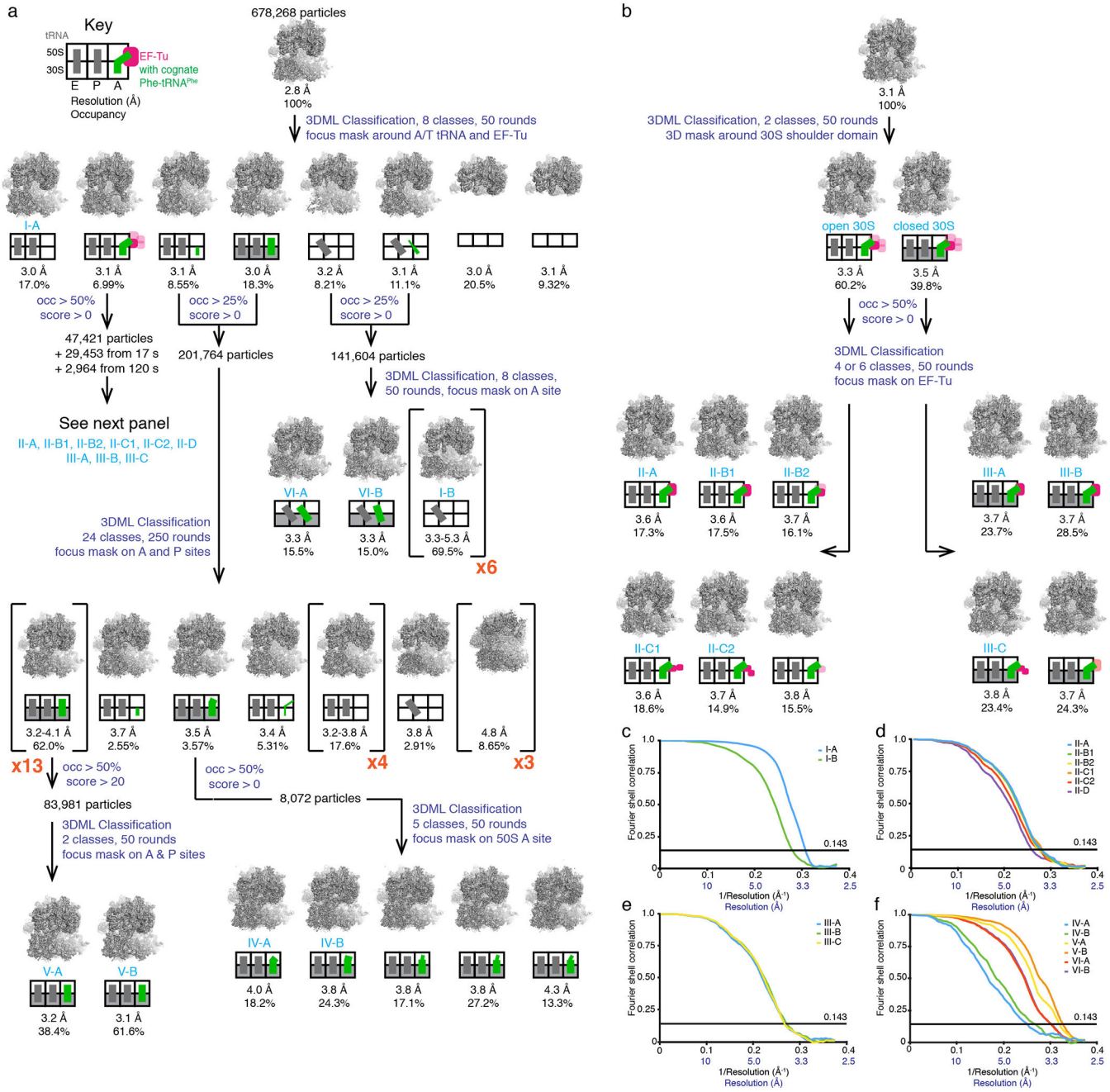

Extended Data Fig. 1.

Classification procedure and FSC curves for maps of cognate ternary complex decoding (**a**) Scheme of the maximum-likelihood classification strategy to obtain the final maps and state occupancies for the cognate 29-s dataset. Transparency for EF-Tu and line-thickness for tRNA depict full/partial occupancy or strong/weak features. Gray shading in 30S subunit indicates the closed 30S subunit conformation. Brackets with red multiplication signs (*e.g. x3*), indicate the number of states that recur, and in such cases the lowest and highest

resolution is listed along with a summed occupancy for all states. (**b**) EF-Tu-bound particles from 17 s, 29 s and 120 s were processed together to obtain final maps for states II-A to III-C. (**c-f**) Fourier shell correlations (FSC) between even- and odd-particle half maps show that average resolutions range from 3.0 to 4.0 Å for modeled maps. (**c**) Substrate ribosome states. (**d**) EF-Tu-bound ribosomes states with an open 30S subunit. (**e**) EF-Tu-bound ribosome states with a closed 30S subunit. (**f**) Accommodation and product ribosome states.

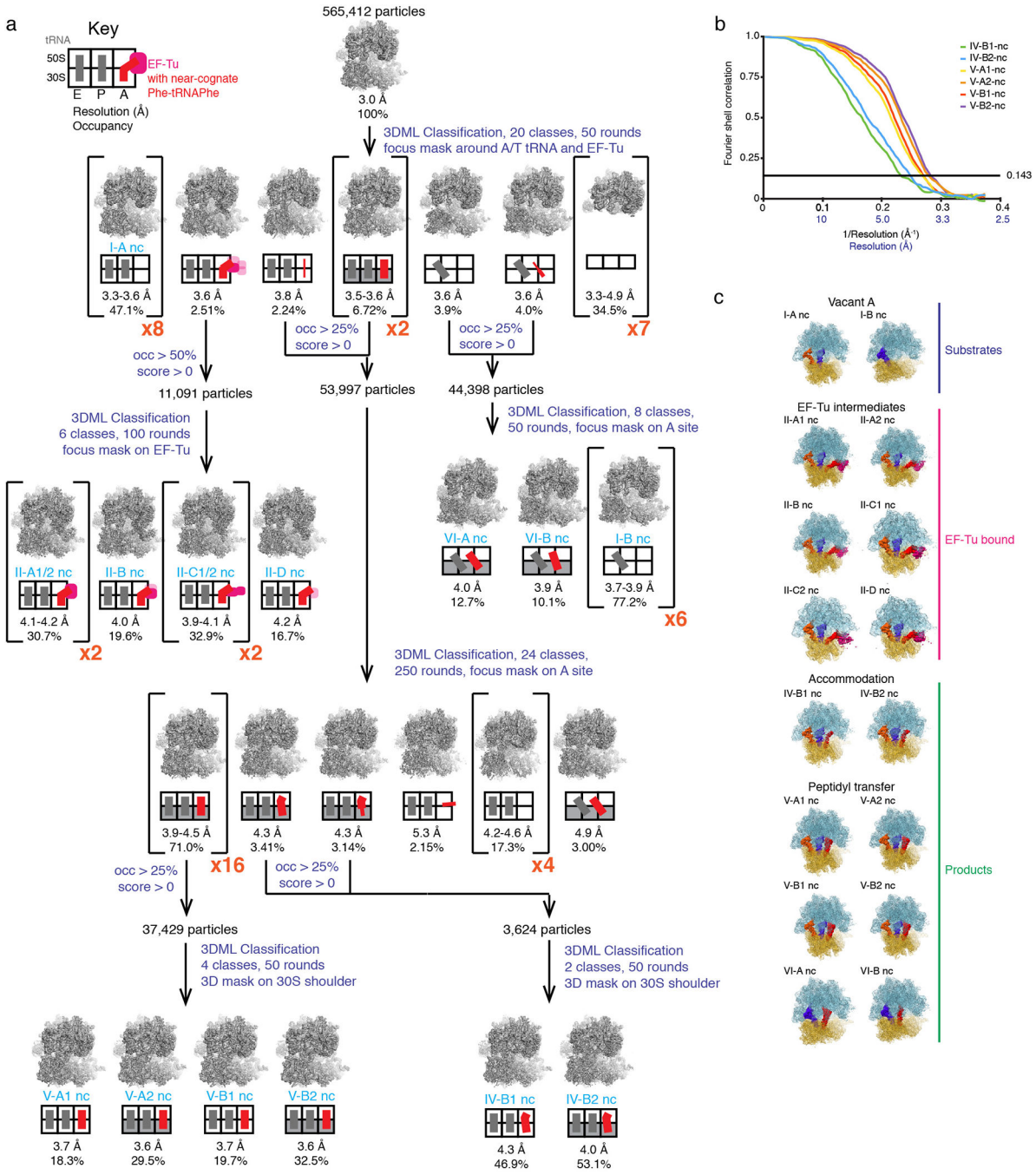

Extended Data Fig. 2.

Classification procedure and FSC curves for maps of near-cognate ternary complex decoding (**a**) Scheme depicts maximum-likelihood classification strategy to obtain the final maps and state occupancies for the near-cognate 30-s dataset. (**b**) Fourier shell correlation (FSC) between even- and odd-particle half maps for near-cognate ribosome states that were modeled. (**c**) Cryo-EM maps for 16 states of the elongation reaction with near-cognate tRNA, and their assignment as substrates, EF-Tu-bound intermediates, or products of the reaction. The maps are colored to show the 50S ribosomal subunit (light blue), 30S ribosomal subunit (yellow), E-tRNA (orange), P-tRNA (dark blue), near-cognate A-tRNA (red), and EF-Tu (magenta).

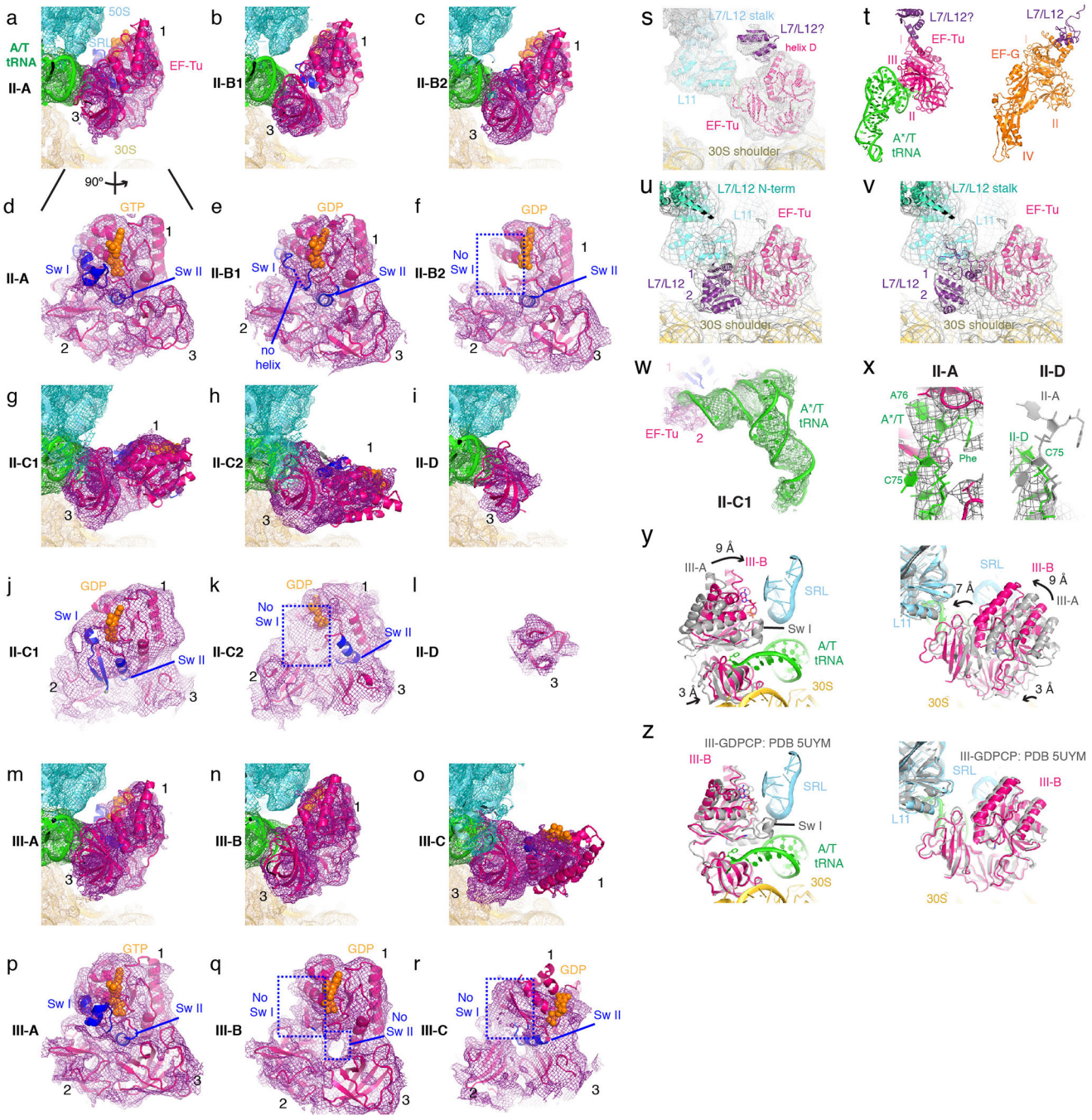

Extended Data Fig. 3.

Cryo-EM density and interactions of EF-Tu. (**a-r**) Density for EF-Tu in 30S-open (II) and 30S-closed (III) conformations is shown relative to the sarcin-ricin loop (SRL) (panels **a-c**, **g-i**, and **m-o**) or at the tRNA interacting face (panels **d-f**, **j-l**, and **p-r**; tRNA is omitted for clarity). Maps were filtered according to local resolution, using blocfilt (**Methods**). Numbers 1–3 indicate domains of EF-Tu. EF-Tu is shown in magenta with switch I region (Sw I) and switch II region (Sw II) shown in blue, tRNA is shown in green, 30S subunit is shown in gold, 50S subunit is shown in cyan. (**a**) Map II-A (shown at 3 σ). (**b**) Map II-B1 (3.25 σ). (**c**)

Map II-B2 (2.5 σ). (**d**) Map II-A has strong density for both Switch I and II regions (2 σ). (**e**) Map II-B1 has weaker density for Switch I (2 σ). (**f**) In map II-B2, density for Switch I is missing even at lower contour levels (shown at 1.5 σ). (**g**) Map II-C1 (1 σ). (**h**) Map II-C2 (1 σ). (**i**) Map II-D has only domain 3 density at low contour levels (0.5 σ). (**j**) Map II-C1 has only weak density for Switch I and II (0.25 σ). (**k**) Map II-C2 is missing ordered density for most of Switch I (0.5 σ). (**l**) Map II-D has weak density only for domain 3 (0.5 σ). (**m**) Map III-A shows EF-Tu away from the SRL when the 30S closure is intermediate (2 σ). (**n**) Map III-B shows EF-Tu next to the SRL, when 30S subunit is in the closed conformation (2 σ). (**o**) Map III-C shows GTPase domain away from the SRL and rotated by ~90° relative to domain 2 (1.5 σ). (**p**) Map III-A has density for both Switch I and II (1.5 σ). (**q**) In map III-B, density for both Switch I and II is missing (1.5 σ). (**r**) Map III-C has weak density for Switch I (1.25 σ). (**s**) Classification with a larger mask around EF-Tu reveals a map with weak density at helix D of domain 1, which corresponds to the binding site for the C-terminus of L7/L12. Map was low-pass filtered to 6 Å and is shown at 1 σ. (**t**) The putative interaction of L7/L12 with domain 1 of EF-Tu (left) differs from that of L7/L12 with domain 1 of EF-G (right). Rigid-body fitted structure of EF-Tu and L7/L12 as in (**a**) was aligned to EF-G from PDB: 4V5F [85] via GTPase domains. (**u-v**) An independent classification strategy yielded a map (shown with 4× binning and at 0.75 σ) with density sufficient to fit a dimer of the L7/L12 C-terminal domain. The density bridges domain 3 of EF-Tu with L11. Model for L7/L12 N-terminus (green cyan) from PDB:1ZAX [86] is shown on both panels. (**u**) Tentative fit utilizes the L7/L12 dimer interface observed in the X-ray crystallographic structure (PDB: 1CTF; [87]). (**v**) Alternatively, two monomers may be docked independently (bottom based on PDB: 1CTF) and top based on PDB: 4V5F.) (**w**) Cryo-EM map II-C1 shows ordered density for A*/T tRNA when EF-Tu domain 1 undocks from the tRNA and SRL, while domain 2 (magenta) remains bound. Map is shown at 3 σ for A*/T tRNA and 2 σ for EF-Tu. (**x**) Comparison between II-A and II-D shows that density is missing for A76 and Phe of Phe-tRNA^{Phe} upon release of EF-Tu domain 2 in II-D. Right panel: Map II-A, filtered via blocfilt and B-factor sharpened (−75 Å^2), with ordered EF-Tu shows strong density for A76 and Phe (2.75 σ). Left panel: Map II-D was filtered via blocfilt and B-factor sharpened (−50 Å^2) and is shown at 0.75 σ to accentuate weak density. A*/T tRNA from II-A is shown in gray for reference after structural superposition of structures via 23S rRNA. (**y**) Comparison of EF-Tu in Structure III-A (resembling a pre-GTP-hydrolysis state, gray, only EF-Tu is shown) and III-B (post-GTP hydrolysis, colored as in Fig. 1) reveals roles of the 30S shoulder in bringing EF-Tu toward the SRL and of L11 in optimally positioning EF-Tu for GTP hydrolysis. Alignment of Structures was achieved by superposition of 23S rRNA. (**z**) Superposition shows similarity of Structure III-B (colored) with 70S• Phe-tRNA^{Phe} •EF-Tu stalled with GDPCP in previous work (PDB: 5UYM; [5]).

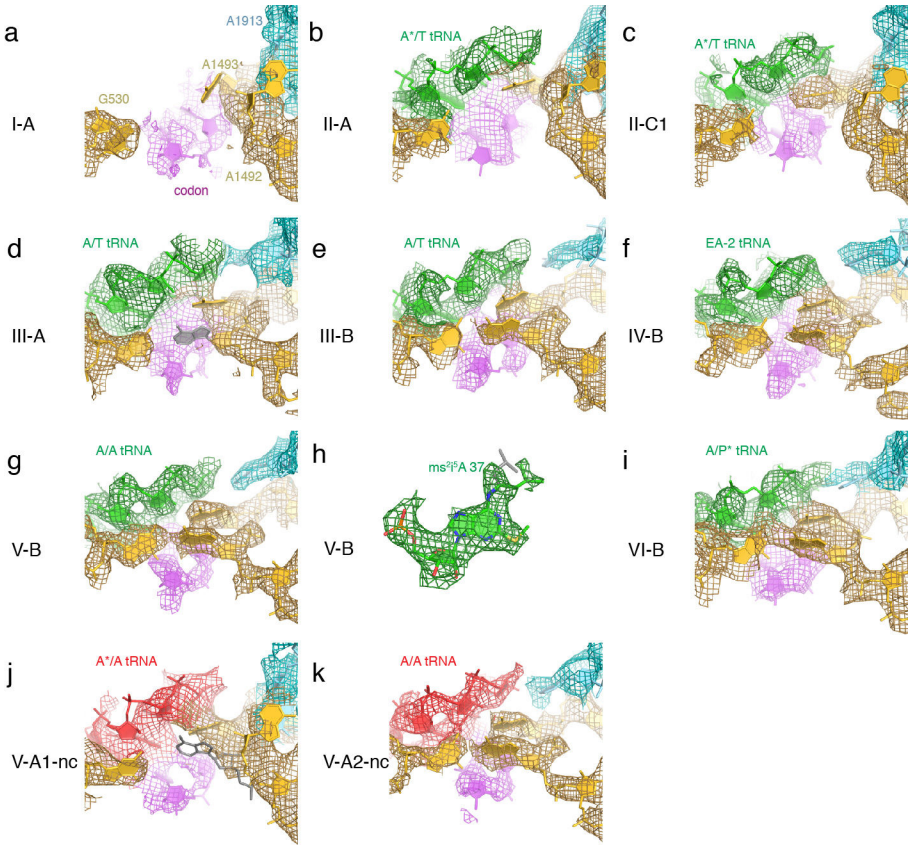

Extended Data Fig. 4.

Cryo-EM density of the decoding center of the open and closed 30S conformations. 16S rRNA is shown in yellow, 23S rRNA is shown in cyan, codon is shown in magenta, cognate tRNA is shown in green and near-cognate tRNA is shown in red. All maps have been local-resolution-filtered using blocfilt and B-factor-sharpened (−75 Å^2). (**a**) Structure I-A with the decoding center in an open conformation; 16S residues of helix 44 including residues 1492–1493 are shown at 2.5 **σ**, G530 of the 16S is shown at 4 **σ**, 23S rRNA residue A1913 at 2.5 **σ**, and the weaker codon density is shown at 1.0 **σ**. (**b**) Structure II-A with the decoding center in an open conformation in the presence of A*/T tRNA; the codon and A*/T tRNA are shown at 2.5 **σ**, h44 is shown at 2.5 **σ**, G530 is shown at 4.5 **σ**, A1913 is shown at 3 **σ**. (**c**) Structure II-C1 with the decoding center in an open conformation in the presence of A*/T tRNA and with EF-Tu in an extended, post-GTP hydrolysis conformation; the codon and A*/T tRNA are shown at 3.75 **σ**, h44 is shown at 2.5 **σ**, G530 is shown at 3 **σ**, A1913 is shown at 2.5 **σ**. (**d**) Structure III-A with the decoding center in an intermediate conformation in the presence of A*/T tRNA; the codon and A*/T tRNA are shown at 3.5 **σ**, h44 is shown at 3.5 **σ**, G530 is shown at 5 **σ**, and A1913 at 2.5 **σ**. (**e**) Structure III-B with a closed conformation of the decoding center in the presence of A/T tRNA; the codon and A/T tRNA are shown at 4.5 **σ**, h44 is shown at 4.5 **σ**, G530 is shown at 5 **σ**, and A1913 is shown at 5 **σ**. (**f**) Structure IV-B with the decoding center in a closed conformation during accommodation; the codon, EA-1 tRNA, A1913 and 16S h44 are shown at 5 **σ**, and G530 is shown at 6 **σ**. (**g**) Structure V-B with the decoding center in a closed conformation in the presence of the accommodated A/A tRNA; the codon and A/A tRNA, 23S rRNA and G530 are shown at 5

σ, and h44 at 4.5 σ. (**h**) Density for the modified nucleotide at position 37, 2-methylthio-N^6-(2-isopentenyl)-adenosine, of the anticodon in V-B (cryo-EM map was filtered with blocfilt and B-factor-sharpened (−100 Å^2) and is shown at 4 σ). (**i**) Structure VI-B with the decoding center in a closed conformation in the presence of A/P* tRNA; the codon, A/T tRNA, h44 and G530 are shown at 3.5 σ, and A1913 at 3 σ. (**j**) Near-cognate Structure V-A1-nc with the decoding center in an open conformation in the presence of A*/A tRNA with the accommodated CCA end; the codon and A*/A tRNA are shown at 3.75 σ, h44 and A1913 are shown at 3.5 σ and G530 is shown at 5 σ. (**k**) Near-cognate Structure V-A2-nc with the decoding center in a closed conformation in the presence of A/A tRNA; the codon and A/A tRNA are shown at 6 σ, h44 is shown at 5 σ, G530 at 7 σ, and A1913 at 3 σ.

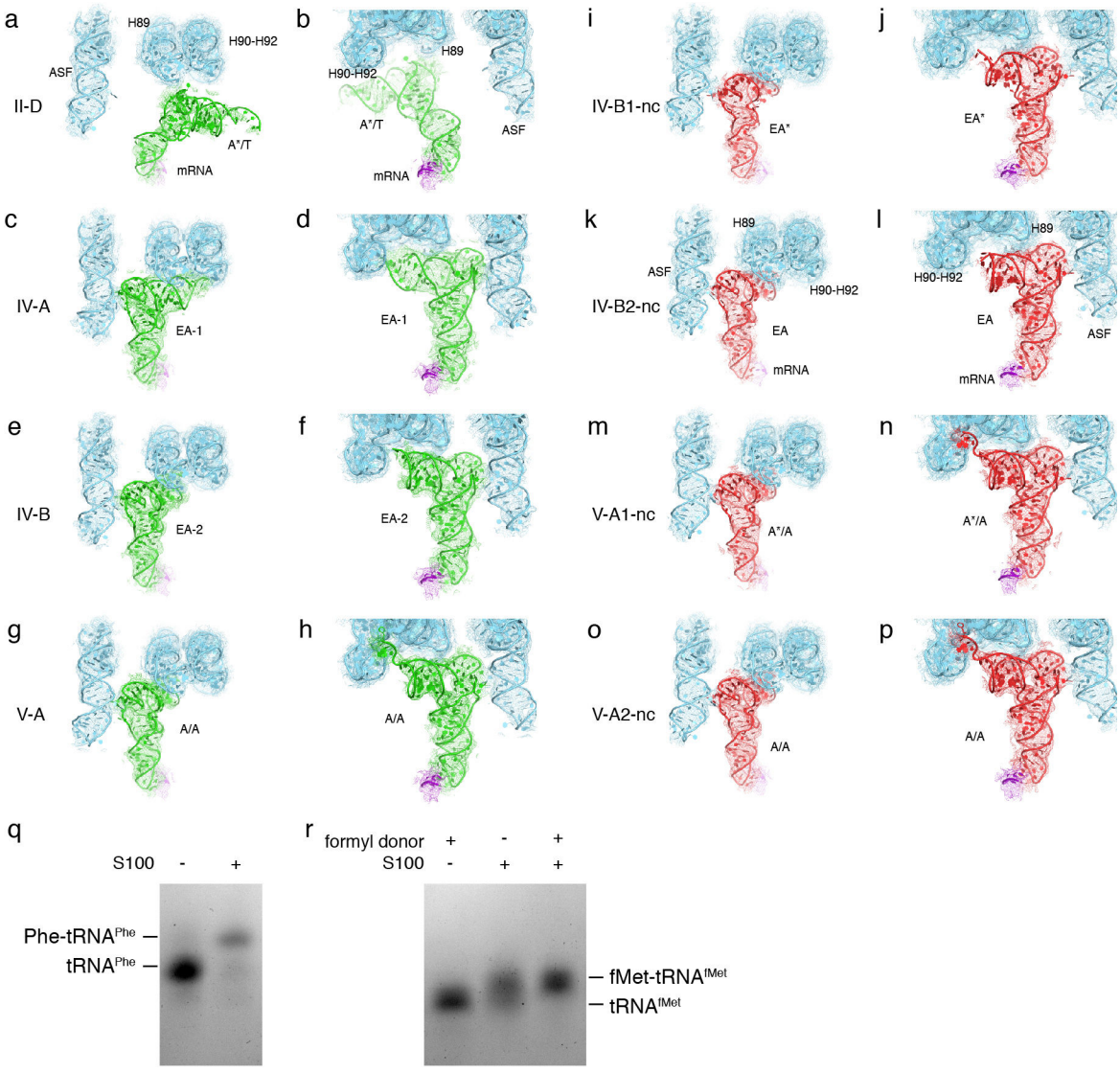

Extended Data Fig. 5.

Cryo-EM density for tRNAs during cognate and near-cognate tRNA decoding. Cognate tRNA is shown in green, near-cognate tRNA is shown in red, 23S rRNA including ASF (residues 860:915), H89 (residues 2450–2500), and H90-H92 (residues 2513:2571) are

shown in cyan, and the mRNA codon is shown in magenta. Cryo-EM maps were local-resolution-filtered using blocfilt. (**a-b**) Structure II-D and cryo-EM map shown at 2 σ. (**c-d**) Structure IV-A and cryo-EM map shown at 3 σ. (**e-f**) Structure IV-B and cryo-EM map shown at 3 σ. (**g-h**) Structure V-A and cryo-EM map shown at 3 σ. (**i-j**) Structure IV-B1-nc and cryo-EM map shown at 2 σ. (**k-l**) Structure IV-B2-nc and cryo-EM map shown at 2 σ. (**m-n**) Structure V-A1-nc and cryo-EM map shown at 3 σ. (**o-p**) Structure V-A2-nc and cryo-EM map shown at 3 σ. (**q**) Charging of $tRNA^{Phe}$ with phenylalanine, as assessed by 6.5% acid-PAGE and methylene-blue staining (see uncropped gel image in Supplementary Information). (**r**) Charging of $tRNA^{fMet}$ by formyl-methionine (as in **q**).

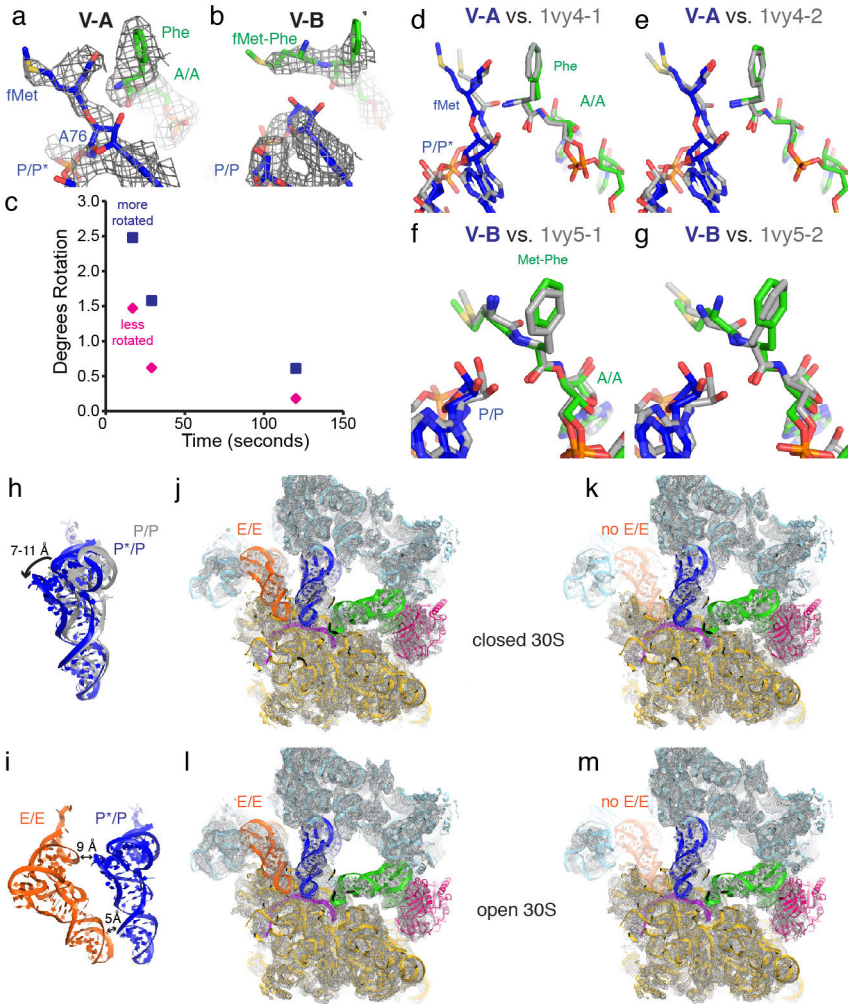

Extended Data Fig. 6.

30S rotation in accommodation states and tRNA conformations in peptidyl-transfer states. (**a**) In state V-A, with a partially rotated 30S subunit, cryo-EM density is consistent with substrate aminoacyl-tRNAs. Cryo-EM map was filtered with blocfilt and B-factor-sharpened (−50 $Å^2$) and is shown at 2.5 σ. (**b**) In state V-B, which is less rotated, cryo-EM density is consistent with product dipeptidyl-tRNA. Cryo-EM map was filtered with blocfilt and B-factor-sharpened (−50 $Å^2$) and is shown at 3.5 σ. (**c**) Change of the 70S conformation in

accommodation intermediates over time. The 30S subunit rotation angle decreases with time in ribosome states with A/A-like tRNA, consistent with accommodation completion in a non-rotated state. Rigid-body docking of 50S subunit, 30S head, 30S shoulder, and 30S body was performed into the cryo-EM maps obtained for the 17- and 120-second time points. Superposition with the 70S•tRNA•EF-Tu•GDPCP structure (PDB: 5UYM, [5]) was achieved by structural alignment of 23S rRNA. Rotation of the 30S body rRNA versus that of non-rotated PDB: 5UYM was determined in Chimera. (**d-g**) Superpositions of the aminoacyl moieties in V-A and V-B with crystallographic structures of the *T. th.* 70S ribosome captured with substrate analogs (PDB: 1VY4) and product analog (PDB: 1VY5) [75]. (**d-e**) Substrate Phe-tRNA^{Phe} in A site (green) and fMet-tRNA^{fMet} (blue) in V-A are shown compared to two 70S structures in the asymmetric unit of PDB: 1VY4 (gray). Superposition was achieved by structural alignment of 23S rRNA. (**f-g**) Product dipeptidyl fMet-Phe-tRNA^{Phe} in the A site (green) and deacylated P-tRNA^{fMet} (blue) in V-B are shown compared to two 70S structures in the asymmetric unit of PDB: 1VY5 (gray). In V-B, formyl group was not resolved. (**h**) P*/P tRNA elbow (blue) in a partially rotated 30S conformation (V-A) is displaced by 7–11 Å toward the E site, relative to its position in the classical-state P/P tRNA (gray; V-B). Superposition of Structures V-A and V-B was achieved by structural alignment of 23S rRNA. (**i**) P*/P tRNA (blue) is shown relative to the E-site tRNA (orange) in structure V-A. (**j-k**) Particle classification yields E-site tRNA-bound (**j**) and vacant (**k**) particles with similar conformations of 30S-domain-closed complexes. Cryo-EM maps with or without E-tRNA (see Methods) were low-pass filtered to 4 Å and B-factor softened (50 Å^2) and are shown at 3.2 σ. (**l-m**) Particle classification yields E-site tRNA-bound (**l**) and vacant (**m**)) particles with similar conformations of 30S-domain-open complexes. Cryo-EM maps with or without E-tRNA (see Methods) prepared as in (**j-k**) are shown at 3 σ.

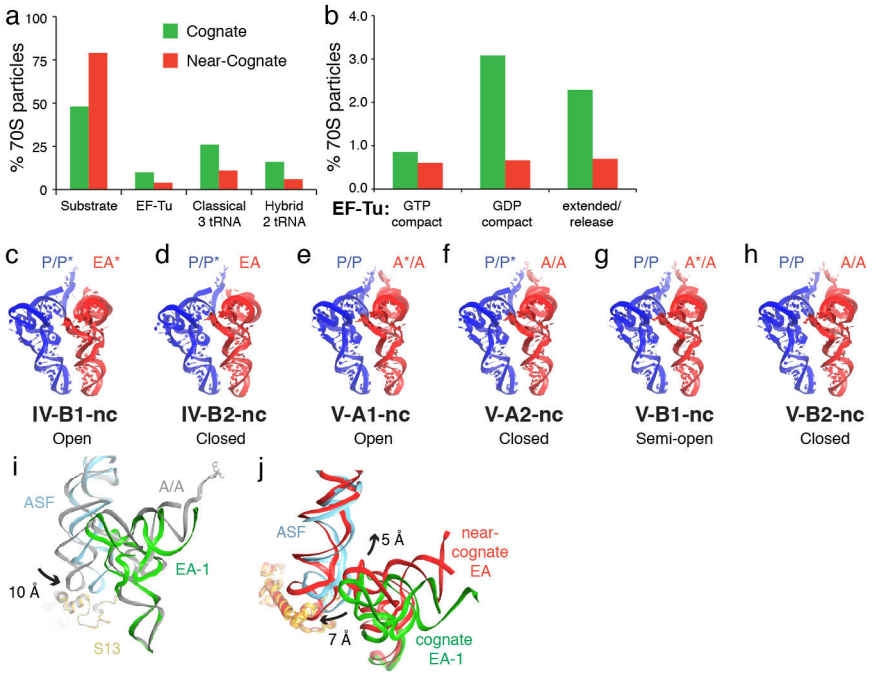

Extended Data Fig. 7.

Differences between near-cognate and cognate structural ensembles. (**a**) Comparison of particle populations in cognate and near-cognate samples (at 30 s) reveals more substrate and less intermediate (EF-Tu) and product states for the near-cognate reaction. (**b**) Near-cognate tRNA-bound EF-Tu is less abundant in GDP-bound states (after GTP hydrolysis) than the cognate complex. (**c-d**) Elbow-accommodated EA tRNAs sample open (**c**) and closed (**d**) 30S conformations. (**e-h**). CCA-accommodated tRNAs sample open and closed 30S conformations. Notably, state V-A1-nc, with an open 30S, shows a destabilized amino acid in the PTC. (**i**) 30S-subunit partial rotation moves the A-site finger (ASF, cyan) in the cognate EA-1 and EA-2 states from their position in the EF-Tu release or accommodated A/A states (gray) allowing tRNA accommodation. (**j**) Near-cognate tRNA (red) accommodation and interactions with the ASF differ from those of cognate tRNA (green).

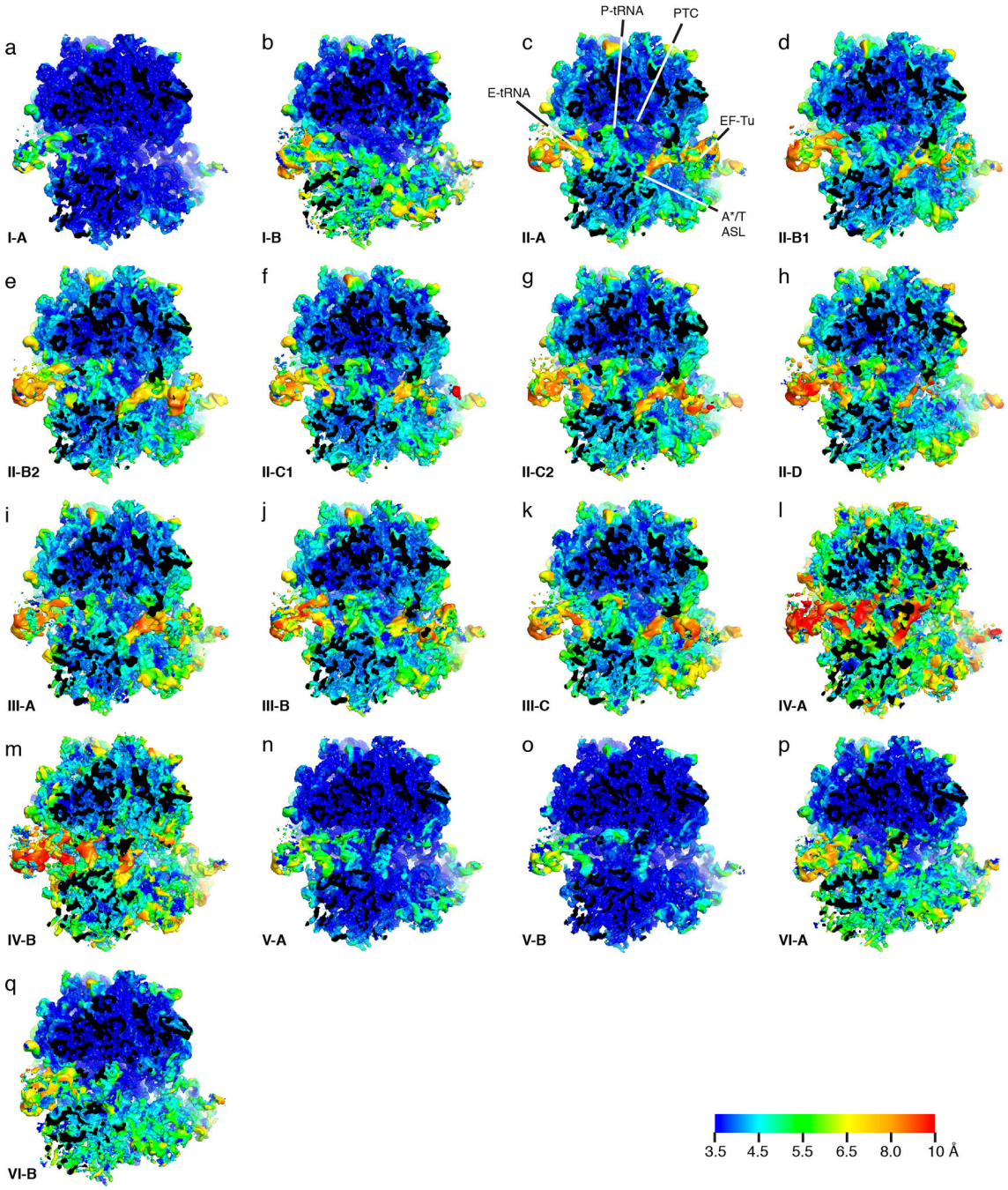

Extended Data Fig. 8.

Local resolutions of each cognate modeled class assessed by blocres (**Methods**).

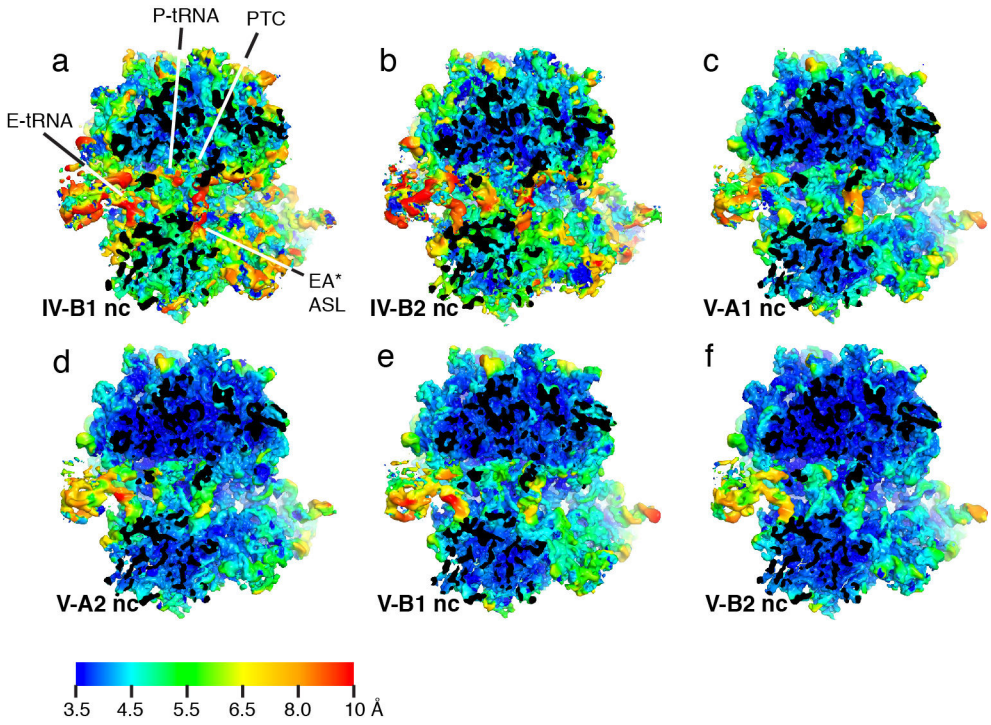

Extended Data Fig. 9.

Local resolutions of each near-cognate modeled class assessed by blocres (**Methods**).

Supplementary Material

Refer to Web version on PubMed Central for supplementary material.

Acknowledgments

We thank Mike Rigney for help with grid preparation and screening at the cryo-EM facility at Brandeis University; Chen Xu and Kangkang Song for data collection at the cryo-EM facility at UMass Medical School; Darryl Conte Jr., Dmitri Ermolenko, Alexei Korennykh and members of the Korostelev laboratory for helpful comments on the manuscript; David Grunwald and Denis Susorov for help with the video. This study was supported by NIH Grants R01 GM106105, R01 GM107465 and R35 GM127094 (to A.A.K.). A.B.L. performed part of this work as a Howard Hughes Medical Institute Fellow of the Helen Hay Whitney Foundation.

Literature Cited

1. Hopfield JJ Kinetic proofreading: a new mechanism for reducing errors in biosynthetic processes requiring high specificity. Proc Natl Acad Sci U S A 71, 4135–4139 (1974). [PubMed: 4530290]
2. Voorhees RM & Ramakrishnan V Structural basis of the translational elongation cycle. Annu Rev Biochem 82, 203–236, doi:10.1146/annurev-biochem-113009-092313 (2013). [PubMed: 23746255]
3. Pavlov MY & Ehrenberg M Substrate-Induced Formation of Ribosomal Decoding Center for Accurate and Rapid Genetic Code Translation. Annu Rev Biophys 47, 525–548, doi:10.1146/annurev-biophys-060414-034148 (2018). [PubMed: 29792818]
4. Rodnina MV, Fischer N, Maracci C & Stark H Ribosome dynamics during decoding. Philos Trans R Soc Lond B Biol Sci 372, doi:10.1098/rstb.2016.0182 (2017).
5. Loveland AB, Demo G, Grigorieff N & Korostelev AA Ensemble cryo-EM elucidates the mechanism of translation fidelity. Nature 546, 113–117, doi:10.1038/nature22397 (2017). [PubMed: 28538735]

6. Fislage M et al. Cryo-EM shows stages of initial codon selection on the ribosome by aa-tRNA in ternary complex with GTP and the GTPase-deficient EF-TuH84A. Nucleic Acids Res 46, 5861–5874, doi:10.1093/nar/gky346 (2018). [PubMed: 29733411]
7. Moazed D & Noller HF Intermediate states in the movement of transfer RNA in the ribosome. Nature 342, 142–148, doi:10.1038/342142a0 (1989). [PubMed: 2682263]
8. Yusupov MM et al. Crystal structure of the ribosome at 5.5 A resolution. Science 292, 883–896 (2001). [PubMed: 11283358]
9. Stark H et al. Visualization of elongation factor Tu on the Escherichia coli ribosome. Nature 389, 403–406, doi:10.1038/38770 (1997). [PubMed: 9311785]
10. Ehrenberg M & Blomberg C Thermodynamic constraints on kinetic proofreading in biosynthetic pathways. Biophys J 31, 333–358, doi:10.1016/S0006-3495(80)85063-6 (1980). [PubMed: 7260292]
11. Pape T, Wintermeyer W & Rodnina M Induced fit in initial selection and proofreading of aminoacyl-tRNA on the ribosome. Embo J 18, 3800–3807 (1999). [PubMed: 10393195]
12. Fischer N et al. Structure of the E. coli ribosome-EF-Tu complex at <3 A resolution by Cs-corrected cryo-EM. Nature 520, 567–570, doi:10.1038/nature14275 (2015). [PubMed: 25707802]
13. Schmeing TM et al. The crystal structure of the ribosome bound to EF-Tu and aminoacyl-tRNA. Science 326, 688–694 (2009). [PubMed: 19833920]
14. Noel JK & Whitford PC How EF-Tu can contribute to efficient proofreading of aa-tRNA by the ribosome. Nat Commun 7, 13314, doi:10.1038/ncomms13314 (2016). [PubMed: 27796304]
15. Sanbonmatsu KY, Joseph S & Tung CS Simulating movement of tRNA into the ribosome during decoding. Proc Natl Acad Sci U S A 102, 15854–15859, doi:0503456102 [pii] 10.1073/pnas.0503456102 (2005). [PubMed: 16249344]
16. Abeyrathne PD, Koh CS, Grant T, Grigorieff N & Korostelev AA Ensemble cryo-EM uncovers inchworm-like translocation of a viral IRES through the ribosome. Elife 5, doi:10.7554/eLife.14874 (2016).
17. Thompson RC, Dix DB, Gerson RB & Karim AM A GTPase reaction accompanying the rejection of Leu-tRNA2 by UUU-programmed ribosomes. Proofreading of the codon-anticodon interaction by ribosomes. J Biol Chem 256, 81–86 (1981). [PubMed: 6108958]
18. Dunkle JA et al. Structures of the bacterial ribosome in classical and hybrid states of tRNA binding. Science 332, 981–984, doi:332/6032/981 [pii] 10.1126/science.1202692 (2011). [PubMed: 21596992]
19. Korostelev A, Trakhanov S, Laurberg M & Noller HF Crystal structure of a 70S ribosome-tRNA complex reveals functional interactions and rearrangements. Cell 126, 1065–1077 (2006). [PubMed: 16962654]
20. Ieong KW, Uzun U, Selmer M & Ehrenberg M Two proofreading steps amplify the accuracy of genetic code translation. Proc Natl Acad Sci U S A 113, 13744–13749, doi:10.1073/pnas.1610917113 (2016). [PubMed: 27837019]
21. Yang H, Perrier J & Whitford PC Disorder guides domain rearrangement in elongation factor Tu. Proteins 86, 1037–1046, doi:10.1002/prot.25575 (2018). [PubMed: 30035820]
22. Kothe U & Rodnina MV Delayed release of inorganic phosphate from elongation factor Tu following GTP hydrolysis on the ribosome. Biochemistry 45, 12767–12774, doi:10.1021/bi061192z (2006). [PubMed: 17042495]
23. Kavaliauskas D et al. Structural dynamics of translation elongation factor Tu during aa-tRNA delivery to the ribosome. Nucleic Acids Res 46, 8651–8661, doi:10.1093/nar/gky651 (2018). [PubMed: 30107527]
24. Berchtold H et al. Crystal structure of active elongation factor Tu reveals major domain rearrangements. Nature 365, 126–132, doi:10.1038/365126a0 (1993). [PubMed: 8371755]
25. Polekhina G et al. Helix unwinding in the effector region of elongation factor EF-Tu–GDP. Structure 4, 1141–1151, doi:10.1016/S0969-2126(96)00122-0 (1996). [PubMed: 8939739]
26. Kjeldgaard M, Nissen P, Thirup S & Nyborg J The crystal structure of elongation factor EF-Tu from Thermus aquaticus in the GTP conformation. Structure 1, 35–50 (1993). [PubMed: 8069622]

27. Voorhees RM, Schmeing TM, Kelley AC & Ramakrishnan V The mechanism for activation of GTP hydrolysis on the ribosome. Science 330, 835–838, doi:330/6005/835 [pii] 10.1126/science.1194460 (2010). [PubMed: 21051640]
28. Kothe U, Wieden HJ, Mohr D & Rodnina MV Interaction of helix D of elongation factor Tu with helices 4 and 5 of protein L7/12 on the ribosome. J Mol Biol 336, 1011–1021, doi:10.1016/j.jmb.2003.12.080 (2004). [PubMed: 15037065]
29. Schuette JC et al. GTPase activation of elongation factor EF-Tu by the ribosome during decoding. EMBO J 28, 755–765, doi:10.1038/emboj.2009.26 (2009). [PubMed: 19229291]
30. Villa E et al. Ribosome-induced changes in elongation factor Tu conformation control GTP hydrolysis. Proc Natl Acad Sci U S A 106, 1063–1068, doi:0811370106 [pii] 10.1073/pnas.0811370106 (2009). [PubMed: 19122150]
31. Pape T, Wintermeyer W & Rodnina MV Complete kinetic mechanism of elongation factor Tu-dependent binding of aminoacyl-tRNA to the A site of the E. coli ribosome. Embo J 17, 7490–7497 (1998). [PubMed: 9857203]
32. Hausner TP, Atmadja J & Nierhaus KH Evidence that the G2661 region of 23S rRNA is located at the ribosomal binding sites of both elongation factors. Biochimie 69, 911–923 (1987).
33. Moazed D, Robertson JM & Noller HF Interaction of elongation factors EF-G and EF-Tu with a conserved loop in 23S RNA. Nature 334, 362–364, doi:10.1038/334362a0 (1988). [PubMed: 2455872]
34. Daviter T, Wieden HJ & Rodnina MV Essential role of histidine 84 in elongation factor Tu for the chemical step of GTP hydrolysis on the ribosome. J Mol Biol 332, 689–699 (2003). [PubMed: 12963376]
35. Maracci C, Peske F, Dannies E, Pohl C & Rodnina MV Ribosome-induced tuning of GTP hydrolysis by a translational GTPase. Proc Natl Acad Sci U S A 111, 14418–14423, doi:10.1073/pnas.1412676111 (2014). [PubMed: 25246550]
36. Koripella RK et al. A conserved histidine in switch-II of EF-G moderates release of inorganic phosphate. Sci Rep 5, 12970, doi:10.1038/srep12970 (2015). [PubMed: 26264741]
37. Ogle JM et al. Recognition of cognate transfer RNA by the 30S ribosomal subunit. Science 292, 897–902 (2001). [PubMed: 11340196]
38. Ogle JM & Ramakrishnan V Structural insights into translational fidelity. Annu Rev Biochem 74, 129–177, doi:10.1146/annurev.biochem.74.061903.155440 (2005). [PubMed: 15952884]
39. Demeshkina N, Jenner L, Westhof E, Yusupov M & Yusupova G A new understanding of the decoding principle on the ribosome. Nature 484, 256–259, doi:10.1038/nature10913 (2012). [PubMed: 22437501]
40. Whitford PC et al. Accommodation of aminoacyl-tRNA into the ribosome involves reversible excursions along multiple pathways. RNA 16, 1196–1204, doi:rna.2035410 [pii] 10.1261/rna.2035410 (2010). [PubMed: 20427512]
41. Jenner L, Demeshkina N, Yusupova G & Yusupov M Structural rearrangements of the ribosome at the tRNA proofreading step. Nat Struct Mol Biol 17, 1072–1078 (2010). [PubMed: 20694005]
42. Frank J & Agrawal RK A ratchet-like inter-subunit reorganization of the ribosome during translocation. Nature 406, 318–322 (2000). [PubMed: 10917535]
43. Noller HF, Lancaster L, Zhou J & Mohan S The ribosome moves: RNA mechanics and translocation. Nat Struct Mol Biol 24, 1021–1027, doi:10.1038/nsmb.3505 (2017). [PubMed: 29215639]
44. Zhang J, Pavlov MY & Ehrenberg M Accuracy of genetic code translation and its orthogonal corruption by aminoglycosides and Mg2+ ions. Nucleic Acids Res 46, 1362–1374, doi:10.1093/nar/gkx1256 (2018). [PubMed: 29267976]
45. Zhang J, Ieong KW, Johansson M & Ehrenberg M Accuracy of initial codon selection by aminoacyl-tRNAs on the mRNA-programmed bacterial ribosome. Proc Natl Acad Sci U S A 112, 9602–9607, doi:10.1073/pnas.1506823112 (2015). [PubMed: 26195797]
46. Gromadski KB & Rodnina MV Kinetic determinants of high-fidelity tRNA discrimination on the ribosome. Mol Cell 13, 191–200 (2004). [PubMed: 14759365]
47. Johansson M, Bouakaz E, Lovmar M & Ehrenberg M The kinetics of ribosomal peptidyl transfer revisited. Mol Cell 30, 589–598, doi:10.1016/j.molcel.2008.04.010 (2008). [PubMed: 18538657]

48. Fu Z et al. Key Intermediates in Ribosome Recycling Visualized by Time-Resolved Cryoelectron Microscopy. Structure 24, 2092–2101, doi:10.1016/j.str.2016.09.014 (2016). [PubMed: 27818103]
49. Kaledhonkar S et al. Late steps in bacterial translation initiation visualized using time-resolved cryo-EM. Nature 570, 400–404, doi:10.1038/s41586-019-1249-5 (2019). [PubMed: 31108498]
50. Nikolay R et al. Structural Visualization of the Formation and Activation of the 50S Ribosomal Subunit during In Vitro Reconstitution. Mol Cell 70, 881–893 e883, doi:10.1016/j.molcel.2018.05.003 (2018). [PubMed: 29883607]
51. Graf M et al. Visualization of translation termination intermediates trapped by the Apidaecin 137 peptide during RF3-mediated recycling of RF1. Nat Commun 9, 3053, doi:10.1038/s41467-018-05465-1 (2018). [PubMed: 30076302]

Literature Cite in Methods and Extended Data

52. Svidritskiy E & Korostelev AA Conformational control of translation termination on the 70S ribosome. Structure 26, 821–828 (2018). [PubMed: 29731232]
53. Lancaster L & Noller HF Involvement of 16S rRNA nucleotides G1338 and A1339 in discrimination of initiator tRNA. Mol Cell 20, 623–632, doi:S1097–2765(05)01676-X [pii] 10.1016/j.molcel.2005.10.006 (2005). [PubMed: 16307925]
54. Walker SE & Fredrick K Preparation and evaluation of acylated tRNAs. Methods 44, 81–86, doi:10.1016/j.ymeth.2007.09.003 (2008). [PubMed: 18241790]
55. Mastronarde DN Automated electron microscope tomography using robust prediction of specimen movements. J. Struct. Biol 152, 36–51, doi:10.1016/j.jsb.2005.07.007 (2005). [PubMed: 16182563]
56. Kremer JR, Mastronarde DN & McIntosh JR Computer Visualization of Three-Dimensional Image Data Using IMOD. J. Struct. Biol 116, 71–76, doi:10.1006/jsbi.1996.0013 (1996). [PubMed: 8742726]
57. Rohou A & Grigorieff N CTFFIND4: Fast and accurate defocus estimation from electron micrographs. J. Struct. Biol 192, 216–221, doi:10.1016/j.jsb.2015.08.008 (2015). [PubMed: 26278980]
58. Chen JZ & Grigorieff N SIGNATURE: A single-particle selection system for molecular electron microscopy. J. Struct. Biol 157, 168–173, doi:10.1016/j.jsb.2006.06.001 (2007). [PubMed: 16870473]
59. Gabashvili IS et al. Solution Structure of the E. coli 70S Ribosome at 11.5 Å Resolution. Cell 100, 537–549, doi:10.1016/S0092-8674(00)80690-X (2000). [PubMed: 10721991]
60. Tang G et al. EMAN2: an extensible image processing suite for electron microscopy. J. Struct. Biol 157, 38–46, doi:10.1016/j.jsb.2006.05.009 (2007). [PubMed: 16859925]
61. Lyumkis D, Brilot AF, Theobald DL & Grigorieff N Likelihood-based classification of cryo-EM images using FREALIGN. J. Struct. Biol 183, 377–388, doi:10.1016/j.jsb.2013.07.005 (2013). [PubMed: 23872434]
62. Wieden HJ, Wintermeyer W & Rodnina MV A common structural motif in elongation factor Ts and ribosomal protein L7/12 may be involved in the interaction with elongation factor Tu. J Mol Evol 52, 129–136 (2001). [PubMed: 11231892]
63. Cornish PV, Ermolenko DN, Noller HF & Ha T Spontaneous intersubunit rotation in single ribosomes. Mol Cell 30, 578–588, doi:S1097–2765(08)00334–1 [pii] 10.1016/j.molcel.2008.05.004 (2008). [PubMed: 18538656]
64. Jenner LB, Demeshkina N, Yusupova G & Yusupov M Structural aspects of messenger RNA reading frame maintenance by the ribosome. Nat Struct Mol Biol 17, 555–560 (2010). [PubMed: 20400952]
65. Nierhaus KH The allosteric three-site model for the ribosomal elongation cycle: features and future. Biochemistry 29, 4997–5008 (1990). [PubMed: 2198935]
66. Dinos G, Kalpaxis DL, Wilson DN & Nierhaus KH Deacylated tRNA is released from the E site upon A site occupation but before GTP is hydrolyzed by EF-Tu. Nucleic Acids Res 33, 5291–5296, doi:10.1093/nar/gki833 (2005). [PubMed: 16166657]

67. Semenkov YP, Rodnina MV & Wintermeyer W The “allosteric three-site model” of elongation cannot be confirmed in a well-defined ribosome system from Escherichia coli. Proc Natl Acad Sci U S A 93, 12183–12188, doi:10.1073/pnas.93.22.12183 (1996). [PubMed: 8901554]
68. Petropoulos AD & Green R Further in vitro exploration fails to support the allosteric three-site model. J Biol Chem 287, 11642–11648, doi:10.1074/jbc.C111.330068 (2012). [PubMed: 22378789]
69. Uemura S et al. Real-time tRNA transit on single translating ribosomes at codon resolution. Nature 464, 1012–1017 (2010). [PubMed: 20393556]
70. Grant T, Rohou A & Grigorieff N cisTEM, user-friendly software for single-particle image processing. Elife 7, doi:10.7554/eLife.35383 (2018).
71. Zivanov J et al. New tools for automated high-resolution cryo-EM structure determination in RELION-3. Elife 7, doi:10.7554/eLife.42166 (2018).
72. Passos DO & Lyumkis D Single-particle cryoEM analysis at near-atomic resolution from several thousand asymmetric subunits. J Struct Biol 192, 235–244, doi:10.1016/j.jsb.2015.10.002 (2015). [PubMed: 26470814]
73. Cardone G, Heymann JB & Steven AC One number does not fit all: mapping local variations in resolution in cryo-EM reconstructions. J Struct Biol 184, 226–236, doi:S1047–8477(13)00208–6 [pii] 10.1016/j.jsb.2013.08.002 (2013). [PubMed: 23954653]
74. Abel K, Yoder MD, Hilgenfeld R & Jurnak F An alpha to beta conformational switch in EF-Tu. Structure 4, 1153–1159 (1996). [PubMed: 8939740]
75. Polikanov YS, Steitz TA & Innis CA A proton wire to couple aminoacyl-tRNA accommodation and peptide-bond formation on the ribosome. Nat Struct Mol Biol 21, 787–793, doi:nsmb.2871 [pii] 10.1038/nsmb.2871 (2014). [PubMed: 25132179]
76. Jin H, Kelley AC & Ramakrishnan V Crystal structure of the hybrid state of ribosome in complex with the guanosine triphosphatase release factor 3. Proc Natl Acad Sci U S A 108, 15798–15803, doi:10.1073/pnas.1112185108 (2011). [PubMed: 21903932]
77. Pettersen EF et al. UCSF Chimera—A visualization system for exploratory research and analysis. Journal of Computational Chemistry 25, 1605–1612, doi:10.1002/jcc.20084 (2004). [PubMed: 15264254]
78. Korostelev A, Bertram R & Chapman MS Simulated-annealing real-space refinement as a tool in model building. Acta Crystallogr D Biol Crystallogr 58, 761–767 (2002). [PubMed: 11976486]
79. Chapman MS Restrained real-space macromolecular atomic refinement using a new resolution-dependent electron-density function. Acta Crystallographica Section A 51, 69–80, doi:10.1107/S0108767394007130 (1995).
80. DeLano WL The PyMOL Molecular Graphics System. (DeLano Scientific, 2002).
81. Emsley P & Cowtan K Coot: model-building tools for molecular graphics. Acta Crystallogr D Biol Crystallogr 60, 2126–2132 (2004). [PubMed: 15572765]
82. Zhou G, Wang J, Blanc E & Chapman MS Determination of the relative precision of atoms in a macromolecular structure. Acta Crystallographica. Section D, Biological Crystallography 54, 391–399 (1998). [PubMed: 9761907]
83. Laurberg M et al. Structural basis for translation termination on the 70S ribosome. Nature 454, 852–857 (2008). [PubMed: 18596689]
84. Adams PD et al. The Phenix software for automated determination of macromolecular structures. Methods (San Diego, Calif.) 55, 94–106, doi:10.1016/j.ymeth.2011.07.005 (2011).
85. Gao YG et al. The structure of the ribosome with elongation factor G trapped in the posttranslocational state. Science 326, 694–699 (2009). [PubMed: 19833919]
86. Diaconu M et al. Structural basis for the function of the ribosomal L7/12 stalk in factor binding and GTPase activation. Cell 121, 991–1004, doi:10.1016/j.cell.2005.04.015 (2005). [PubMed: 15989950]
87. Leijonmarck M & Liljas A Structure of the C-terminal domain of the ribosomal protein L7/L12 from Escherichia coli at 1.7 A. J Mol Biol 195, 555–579 (1987). [PubMed: 3309338]

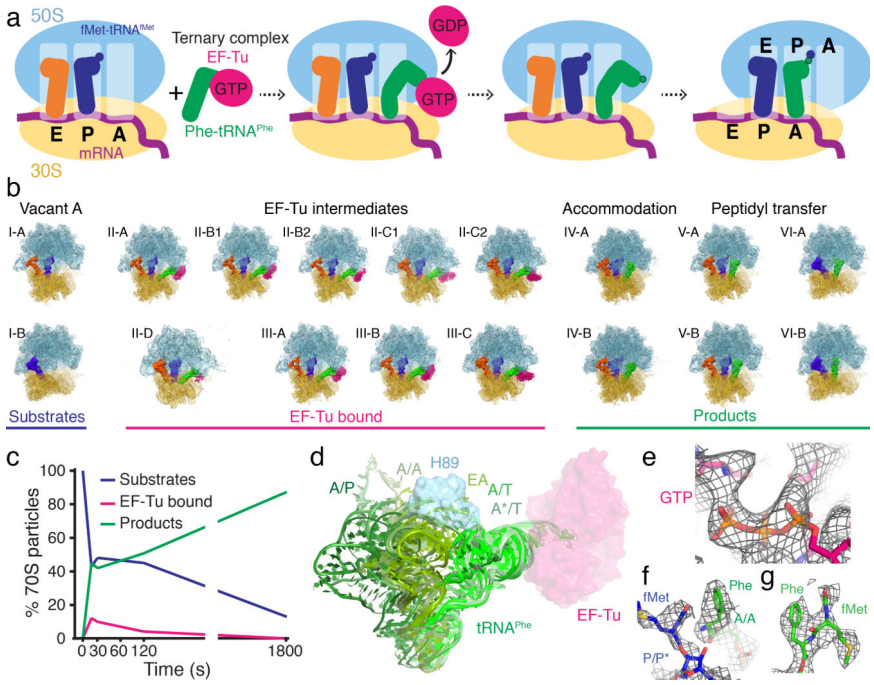

Fig. 1.

Cryo-EM of an elongation event reveals structural intermediates. (**a**) Scheme of the reaction of initiation 70S•fMet-tRNA^{fMet} complex with cognate Phe-tRNA^{Phe}•EF-Tu•GTP complex to form dipeptidyl fMet-Phe-tRNA. (**b**) Cryo-EM maps for 17 states of the elongation reaction, and their assignment as substrates, EF-Tu-bound intermediates, or products of the reaction. The maps are colored to show the 50S ribosomal subunit (light blue), 30S ribosomal subunit (yellow), E-tRNA (orange), P-tRNA (dark blue), A-tRNA (green), and EF-Tu (magenta). (**c**) Relative abundance of substrates, EF-Tu intermediates, and products over time, obtained from particle distributions in cryo-EM datasets. (**d**) Conformations of the incoming tRNA in 17 structures, starting from EF-Tu bound A*/T states (light green tRNA and magenta EF-Tu) to elbow-accommodated (EA) to pre-translocation A/P states (dark green). (**e**) Density (mesh) consistent with GTP in EF-Tu GTPase center of a transient early state of mRNA decoding (open 30S). (**f**) Cryo-EM density of a transient state in the peptidyl transferase center consistent with aminoacyl-tRNA substrates. (**g**) Cryo-EM density for fMet-Phe dipeptidyl-tRNA, the product of peptidyl transfer.

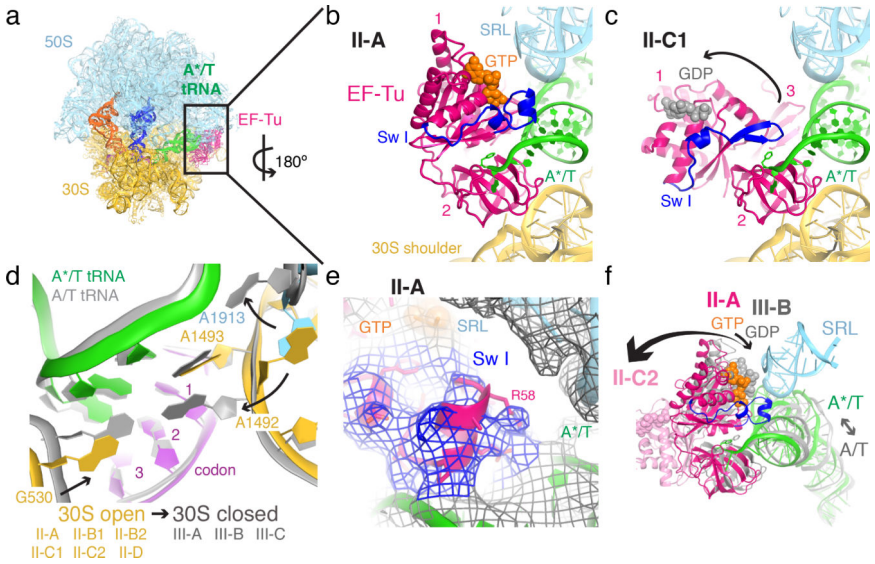

Fig. 2.

EF-Tu and ribosome rearrangements during mRNA decoding. (**a**) Overview of the 70S ribosome bound with ternary complex of Phe-tRNA^{Phe}•EF-Tu•GTP (Structure II-A). (**b**) Compact EF-Tu•GTP with the ordered switch I region (Sw I; blue) is separated from the sarcin-ricin loop (SRL; cyan) on the ribosome with the open 30S conformation (Structure II-A). (**c**) Extended EF-Tu with domain 1 separated from tRNA (arrow) and with a reorganized switch I region (Structure II-C1). (**d**) Rearrangements in the decoding center are coupled with 30S domain closure (shoulder shift) in the presence of EF-Tu. Structures II-A (colored) and III-B (gray) are shown. (**e**) Cryo-EM density showing EF-Tu with an ordered switch I region in the open 30S state (II-A). (**f**) GTP (orange spheres) is hydrolyzed (small black arrow), as the decoding center accepts the tRNA (gray arrow; closed 30S), bringing domain 1 to the SRL (cyan). The disordering and refolding of Sw I (blue) and movement of domain 1 away from tRNA (larger black arrows) occur as the tRNA continues sampling open (A*/T) and closed (A/T) 30S conformations. EF-Tu from II-A (magenta), III-B (gray), and II-C2 (light pink) is shown along with tRNA from II-A (A*/T, colored) and III-B (A/T, gray).

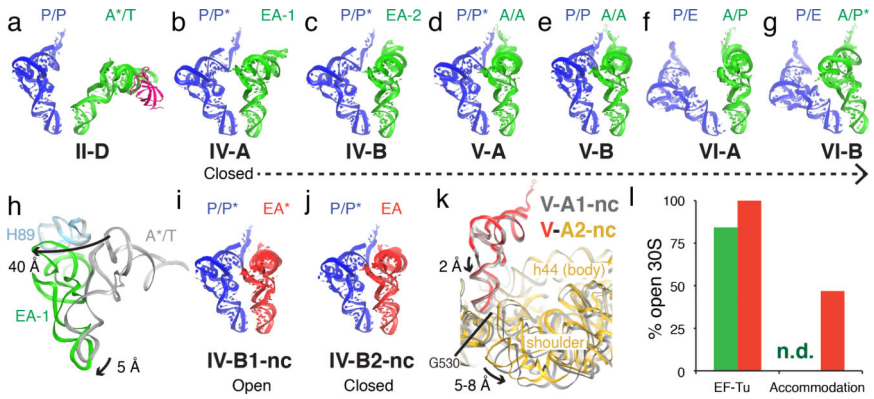

Fig. 3. Differences between cognate (green) and near-cognate (red) tRNA accommodation.

(**a-g**) Cognate tRNA after EF-Tu release samples closed 30S conformations from accommodation to peptidyl transfer to pre-translocation states: (**a**) EF-Tu domain 3 (magenta) is last to release from A*/T tRNA (green). (**b**) Elbow-accommodated tRNA EA-1 in the ribosome with a partially rotated 30S subunit (~2.5°). (**c**) Elbow-accommodated tRNA EA-2 is closer to the A site but the CCA end is not accommodated in the 50S A site. (**d**) The CCA end of A tRNA is inserted into the PTC, while the 30S subunit is partially rotated (also Fig. 1f). (**e**) Dipeptidyl-tRNA in the A site with the less rotated 30S subunit (Extended Data Fig. 6b). (**f-g**) Pre-translocation hybrid-state dipeptidyl-tRNA in the 70S with the fully rotated 30S subunit and different elbow positions of the A/P and A/P* tRNA (as defined in Supplementary Information). (**h**) During accommodation, partial 30S rotation depresses tRNA and allows the tRNA to bypass H89. (**i-j**) Near-cognate tRNA in elbow-accommodated states (IV-B1-nc, IV-B2-nc) sample open (**i**) and closed (**j**) 30S conformations. (**k**) Near-cognate tRNA with accommodated CCA end samples open and closed 30S conformations, coupling the shoulder movement with tRNA destabilization. (**l**) The 30S decoding center samples open 30S conformations with near-cognate tRNA in both EF-Tu-bound and accommodation structures (n.d. not detected for cognate tRNA).

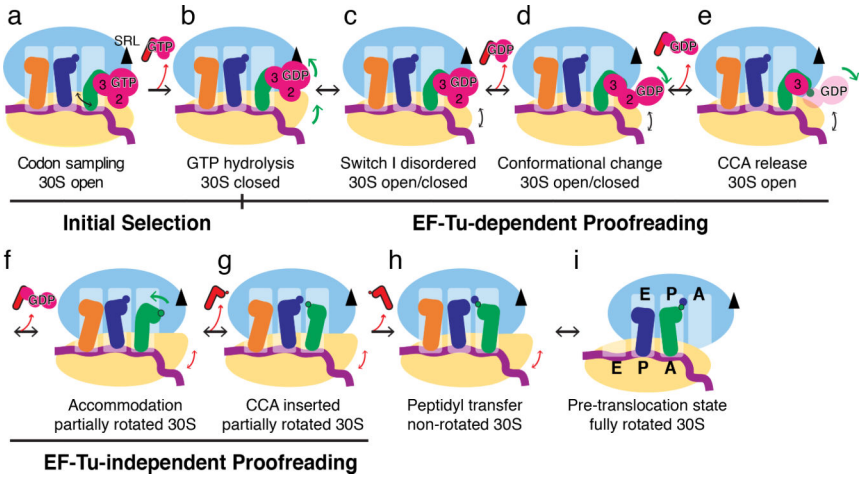

Fig. 4.

Schematic of mRNA decoding. Black arrows denote events and conformational changes (EF-Tu rearrangements, 30S domain closure, and/or tRNA or EF-Tu dissociation) on both cognate (green tRNA) and near-cognate (red tRNA) decoding complexes. Green and red arrows denote events predominant for cognate and near-cognate complexes, respectively.